Remodeling the tumor immune microenvironment through hydrogel encapsulated G-Rh2 *in situ* vaccine and systemic immunotherapy

Chunhua Li [a,1], Dan Lei [a,1], Yudong Huang [d,1], Yuanhao Jing [a], Wanru Wang [a], Lanqi Cen [e], Zijian Wei [a], Anni Chen [a], Xiaoyu Feng [a], Yushu Wang [d], Lixia Yu [b,c], Ying Chen [d,**], Rutian Li [a,b,c,*]

[a] *The Comprehensive Cancer Center, Nanjing Drum Tower Hospital, Clinical College of Nanjing Drum Tower Hospital, Nanjing University of Chinese Medicine, Nanjing, 210008, China*
[b] *The Comprehensive Cancer Center of Nanjing Drum Tower Hospital, The Affiliated Hospital of Nanjing University Medical School, Nanjing, 210008, China*
[c] *Clinical Cancer Institute of Nanjing University, Nanjing, 210008, China*
[d] *State Key Laboratory of Organic Electronics and Information Displays & Institute of Advanced Materials (IAM), Nanjing University of Posts & Telecommunications, Nanjing, 210023, China*
[e] *The Comprehensive Cancer Center, China Pharmaceutical University Nanjing Drum Tower Hospital, Nanjing, 210008, China*

ARTICLE INFO

ABSTRACT

Ginsenoside Rh2 (G-Rh2) is a vital bioactive compound in Traditional Chinese Medicine, celebrated for its strong pharmacological properties, particularly its potent antitumor effects. However, its poor water solubility and limited bioavailability have necessitated the development of a novel drug delivery method. In this study, we utilized an indocyanine green carboxylic acid-hydroxypropyl cellulose-abietic acid-bovine serum albumin hydrogel (ICG-HPC-AA/BSA hydrogel) as a tumor *in situ* vaccine to enhance the permeability, retention, and tumor-targeted therapeutic efficacy of G-Rh2. We examined the therapeutic impact of a G-Rh2-loaded hydrogel combined with systemic PD-1 antibody treatment in murine models of H22 liver cancer and CT26 colon cancer. Additionally, we explored the immune microenvironment of the tumors influenced by this *in situ* vaccination strategy.

1. Introduction

Cancer immunotherapy has developed over more than a century, with rapid acceleration since the success of monoclonal antibodies (mAbs) targeting the inhibitory immune checkpoint blockade (ICBs), specifically PD-1, PD-L1 (programmed cell death-ligand 1, PD-L1) and CTLA4 (Cytotoxic T lymphocyte associate protein-4, CTLA4) [1]. Recent advances have led to significant advancements in cancer treatment using ICBs. For instance, combination therapy with atezolizumab and bevacizumab has shown improved overall survival rates in patients with liver cancer compared with sorafenib [2]. Similarly, nivolumab, pembrolizumab, and ipilimumab have shown promising outcomes in some colon cancer patients [3]. However, PD-1 inhibition is primarily observed in colon cancers with microsatellite instability and mismatch repair defects. For patients with liver and colon cancers with limited responses to immunotherapy, a combined strategy that enhances the tumor immune microenvironment in conjunction with ICBs may increase the effectiveness of the immune response.

The efficacy of PD-1 antibody therapy is predominantly dependent on the tumor microenvironment (TME). Consequently, enhancing the antitumor effectiveness of PD-1 mAbs by modulating the immunosuppressive microenvironment has attracted significant attention from the research community. Recently, tumor vaccines have advanced rapidly, including cell vaccines [4], DNA vaccines [5], mRNA vaccines [6], polypeptide vaccines [7], oncolytic virus vaccines [8], engineered bacterial vaccines [9], and others. Among these, *in situ* vaccines have

attracted increasing interest from researchers. *In situ* tumor vaccines enhance the local antigenicity of the tumor, promote dendritic cell-mediated antigen presentation, increase immune cell infiltration, regulate the tumor microenvironment, and initiate tumor-specific immune responses. Compared to neoantigen vaccines, *in situ* vaccines eliminate the need for personalized antigen detection and customized antigen peptide synthesis, making them more suitable for clinical applications. Implementing *in situ* vaccines relies primarily on strategies such as radiotherapy and intra-tumoral immune injections. Successful outcomes have been reported for intra-tumoral injections involving bacteria and bacterial toxins, oncolytic viruses and molecules, monoclonal antibodies, cytokines, and immune cells [1], among others. The inflammatory response induced by the intra-tumoral injection of bacteria or viruses may be pronounced, potentially leading to fever or allergic reactions, making the selection of injection agents critical. Traditional Chinese medicine monomers have consistently exhibited promise as antitumor agents. Network pharmacological studies have identified numerous traditional Chinese medicine monomers capable of enhancing the tumor immune microenvironment, such as arsenic trioxide [10], celastrol [11], curcumin [12], and ginsenoside Rh2 [13]. Ginsenoside metabolites, specifically ginsenosides Rg3 and C-K, can inhibit the binding between PD-1 and PD-L1 [14]. This discovery suggests that these metabolites have potential as candidate drugs for blocking the PD-1/PD-L1 interaction. Ginsenoside Rh2, a primary metabolite of ginsenosides, interacts with various signal transduction pathways, including TGF-β1/Smad, STAT3, and NF-κB. It functions as an immunomodulator in both physiological and pathological processes. Its multifaceted role is crucial for enhancing immunity and activating the tumor's immune microenvironment.

In situ vaccine technology, which relies on local tumor administration, faces challenges, such as inadequate local drug concentration and rapid drug clearance. A viable solution to these limitations is the implementation of drug delivery systems. Among various drug delivery systems, hydrogels are notable three-dimensional polymer materials that use water as a dispersion medium [15]. Hydrogels can encapsulate various antigens or immunomodulators, counteract immunosuppression, and stimulate immune responses. They also protect the encapsulated components from degradation, thereby enhancing their therapeutic efficacy in tumors with low immunogenicity [16]. The role of hydrogels offers a practical strategy for enhancing clinical autologous cancer vaccines, and this approach helps reverse immune desertification [17]. Various materials are currently used as drug carriers. An ideal material for clinical applications should exhibit several advantageous traits: (1) good biocompatibility and biodegradability, (2) biological controllability, (3) exceptional drug-loading capacity [18,19], (4) minimal invasiveness and improved prognosis [20]. In response to these considerations, we developed a thermo-responsive injectable hydrogel (ICG-HPC-AA/BSA hydrogel) crosslinked through a hydrogen bond network and ICG-COOH incorporation. We used a hydrogel to formulate an *in situ* vaccine by entrapping G-Rh2, which was administered to mice as a tumor vaccine. G-Rh2, despite its potential for antitumor applications, is constrained by intrinsic limitations, such as poor water solubility, low stability in the gastrointestinal tract and bloodstream, and limited bioavailability. The primary constituents of the hydrogel, hydroxypropyl cellulose (HPC) and bovine serum albumin (BSA), are extensively used biocompatible polymers. Additionally, hydrophobic fragments of abietic acid (AA) were introduced to enhance HPC performance. The ICG-HPC-AA/BSA hydrogel demonstrated the capacity for sustained release of the G-Rh2 drug, effectively overcoming the issues of needle blockage and enabling deep tissue penetration around the implant site. Therefore, it is highly suitable as a carrier for tumor *in situ* vaccines. G-Rh2 and ICG-HPC-AA/BSA hydrogels can be used as tumor vaccines *in situ* combined with the systemic administration of PD-1 antibody to treat tumors.

In this study, we selected liver cancer and colon cancer as models, representing different types of tumors with distinct immune microenvironments. Initially, the immune microenvironment of liver cancer is highly constrained by the liver's inherent immune tolerance characteristics. Within the liver, there are immunosuppressive cells such as Kupffer cells, hepatic dendritic cells, regulatory T cells, and myeloid-derived suppressor cells. These cells help the tumor evade immune surveillance by upregulating immune checkpoint molecules (such as PD-L1 and CTLA-4) and inducing immune tolerance [21]. In contrast, the immune microenvironment of colon cancer exhibits more complex features. It contains various immune cells, including macrophages, dendritic cells, T cells, and NK cells [22]. Due to the higher distribution of macrophages in the liver, we conducted a detection of M1-type macrophages in liver cancer tissues. Given the more complex immune microenvironment of colon cancer, which involves a broader range of immune cell populations, we paid special attention to the distribution of immune cells such as macrophages, dendritic cells, and T lymphocytes. It is of great value to explore the influence of the immune microenvironment on the different immune characteristics of liver and colon cancers using this combination treatment strategy. In this study, we characterized the ICG-HPC-AA/BSA hydrogel, assessed the in vitro toxicity of the G-Rh2-loaded hydrogel in liver and colon cancer cells, and explored the effect of the G-Rh2-loaded hydrogel combined with the PD-1 antibody in the treatment of liver and colon cancer in mice and their tumor immune microenvironment (Scheme 1).

2. Results and discussion

### 2.1. Detection of gelling time for ICG-HPC-AA/BSA hydrogel

The hydrogel was in the liquid state before and during injection. Shortly after injection, it transformed into a gel state upon heating. Within the temperature range of 4–60 °C, both the ICG-HPC-AA solution and the BSA solution remained in their liquid form. Table 1 showed that when the ICG-HPC-AA solution (Fig. 1) and BSA solution were combined under acidic conditions (pH4) and heated to 37 °C, rapid gelation was observed at an ICG-COOH concentration of 3 wt‰ and a ratio of HPC-AA to BSA of 5:5.

2.2. Optical characteristics of ICG-HPC-AA/BSA hydrogel

The optical properties of the ICG-HPC-AA/BSA hydrogel and the ICG solution were examined using near-infrared ultraviolet–visible (NIR-UV-VIS) spectrum analysis, including both absorption and fluorescence measurements (Fig. 2D). The results demonstrated minimal interactions between ICG-COOH and the hydrogel. A strong NIR absorption peak was observed at 788 nm, which increased with the ICG content in the hydrogel, indicating a high photothermal potential under 808 nm laser irradiation. The fluorescence spectra of both the ICG solution and ICG-HPC-AA/BSA hydrogel (Fig. 2E and F) showed maximum emission at 807 nm, allowing for deep tissue penetration during in vivo fluorescence imaging. Therefore, the ICG-HPC-AA/BSA hydrogel exhibited strong NIR absorption and intense fluorescence emission, as evidenced by the NIR-UV-VIS absorption and fluorescence spectra.

2.3. Thermal response characteristics of ICG-HPC-AA/BSA hydrogel

Initially, the temperature changes in various materials under 808 nm laser irradiation were investigated (Fig. S1). To further assess the photothermal performance of the ICG-HPC-AA/BSA hydrogel, it was exposed to an 808 nm laser at different power densities for 10 min. As shown in the figures (Fig. 2G and H), the hydrogel temperature increased with higher power densities, demonstrating a positive correlation. The peak temperature of the hydrogel increased in proportion to the concentration of ICG-COOH. These findings highlight the promising photothermal properties of the ICG-HPC-AA/BSA hydrogel. Furthermore, the ICG-HPC-AA/BSA hydrogel with 1 % mass fraction of G-Rh2 experienced a 1-min delay during the heating process, without affecting
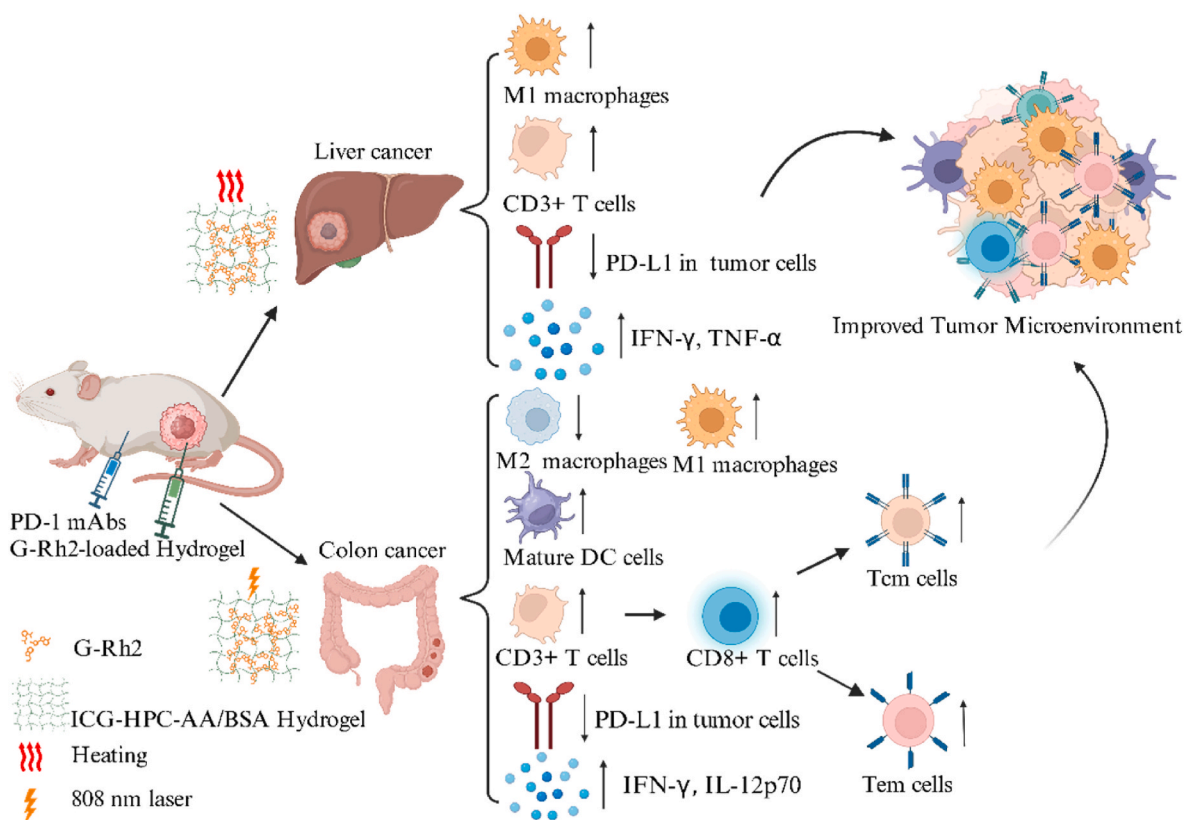
Scheme 1. Schematic diagram illustrating the comprehensive strategy of G-Rh2-loaded hydrogel combined with PD-1 antibody, which is used to explore the immune microenvironments of liver and colon cancer. G-Rh2-loaded hydrogel combined with PD-1 antibody can promote the infiltration of M1 macrophages and CD3+ T cells into the microenvironment of mouse liver cancer, reduce the expression of PD-L1 on liver cancer cells, and enhance the secretion of IFN-γ and TNF-α in mice. G-Rh2-loaded hydrogel, with 808 nm laser irradiation, combined with PD-1 antibody can promote the infiltration of M1 macrophages, mature DC cells, T_{CM} cells, and T_{EM} cells into the microenvironment of mouse colon cancer, reduce the expression of PD-L1 on colon cancer cells and the proportion of M2 macrophages, and enhance the secretion of IFN-γ and IL-12p70 in mice. Programmed Death Protein 1, PD-1; Programmed Death-Ligand 1, PD-L1; Dendritic cells, DC cells; Central memory T cells, T_{CM} cells; Effector memory T cells, T_{EM} cells; Ginsenoside Rh2, G-Rh2; Indocyanine green carboxylic acid-hydroxypropyl cellulose-abietic acid-bovine serum albumin hydrogel, ICG-HPC-AA/BSA hydrogel. (The components were from BioRender (https://biorender.com/)).

Table 1
Detection of gelling time for ICG-HPC-AA/BSA hydrogel.

ICG	HPC-AA	BSA	ICG-HPC-AA/BSA Hydrogels	
Concentration (wt‰)	Concentration (wt %)	Concentration (wt %)	T_{gel} (°C)	Gelling time (s)
3.0	3.0	7.0	37	372
3.0	5.0	5.0	37	90
3.0	7.0	3.0	36	181
5.0	3.0	7.0	37	342
5.0	5.0	5.0	36	106
5.0	7.0	3.0	36	198
7.0	3.0	7.0	36	366
7.0	5.0	5.0	36	114
7.0	7.0	3.0	35	203

the formation of the hydrogel's highest thermal response temperature (Fig. S8).

2.4. Rheological behavior of 5 ‰ ICG-HPC-AA/BSA hydrogel

The hydrogel exhibited low viscosity when the loss modulus (G″) was greater than the storage modulus (G′). At the point where G′ equaled G″, known as the intersection of the two moduli, the hydrogel reached its gel point, marking the transition from a sol to a gel state. The hydrogel behaved as a solid-state gel once the storage modulus exceeded the loss modulus (G'>G″). The rheological performance plots (Fig. 2J)

demonstrated that the 5 ‰ ICG-HPC-AA/BSA hydrogel with varying ratios achieved the sol/gel transition within 6 min at 37 °C under pH = 4 conditions. This transition was significantly faster compared to the simple BSA solution, which took 5–6 h to gel at 60 °C. This difference highlights the superior ability of the 5 ‰ ICG-HPC-AA/BSA hydrogel to rapidly transition from a liquid to a gel state under conditions similar to body temperature. In addition, the 5 ‰ ICG-HPC-AA/BSA hydrogel loaded with 1 % mass fraction of G-Rh2, under the condition of HPC-AA: BSA at a ratio of 5:5, also achieved the sol-gel transition within 6 min at 37 °C (Fig. S9), just like the 5 ‰ ICG-HPC-AA/BSA hydrogel. This also indicates that the addition of G-Rh2 has no significant impact on the rheological properties of the 5 ‰ ICG-HPC-AA/BSA hydrogel.

2.5. In vitro release study of G-Rh2-loaded ICG-HPC-AA/BSA hydrogel

We assessed G-Rh2 content under various pH conditions and found that pH had no significant effect on G-Rh2 content (Fig. S2). Consequently, G-Rh2 was effectively loaded into the ICG-HPC-AA/BSA hydrogel at pH 5.6. We introduced the Chinese medicinal monomer G-Rh2 into the ICG-HPC-AA/BSA hydrogel to explore its antitumor efficacy and examined its release kinetics. We determined the encapsulation efficiency and drug loading according to the standard curve of G-Rh2 (y = 1402.2x + 257.77). The drug loading and encapsulation efficiency of G-Rh2-loaded hydrogel using high-performance liquid chromatography (HPLC) were 4.11 % and 97.44 % respectively. The drug release curve (Fig. 2I) indicated that approximately 25 % of the G-Rh2 was released from the hydrogel within the first 24 h. Subsequently, the remaining
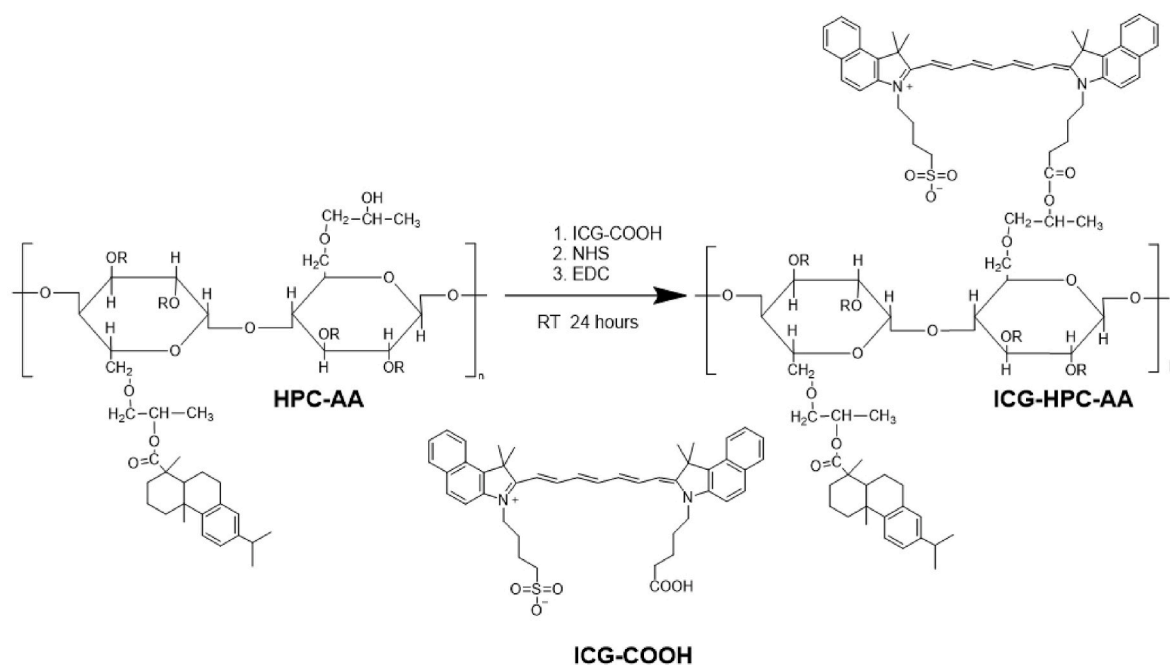
Fig. 1. Synthesis of ICG-HPC-AA solution.

drug content was gradually released over approximately 6 days. These results highlight the ability of the hydrogel to sustain the release of G-Rh2, potentially maintaining its antitumor effect for at least one week. This sustained-release capability indicated the potential of this hydrogel for in vivo therapeutic applications.

2.6. Gelled photograph of ICG-HPC-AA/BSA hydrogel

In vitro, the 5 ‰ ICG-HPC-AA/BSA solution was observed to maintain a liquid state at 25 °C (Fig. 2A) and the same solution transformed into a hydrogel state at 37 °C (Fig. 2B). ICG-HPC-AA/BSA solution forms a stable hydrogel in vitro. We injected the G-Rh2-loaded ICG-HPC-AA/BSA hydrogel into mice, and as a result, we found that a well-formed hydrogel could be established within the mice (Fig. 2C), indicating that the hydrogel possesses good gelation capability in vivo.

2.7. Performance test of ICG-HPC-AA/BSA hydrogel

The stability of the hydrogel was observed in PBS solutions with different pH values. As shown in Fig. 3A, we observed for 30 h and found that the ICG-HPC-AA/BSA hydrogel can maintain a stable gel state in PBS solutions with pH values of 3, 7, and 8. Therefore, we believe that this hydrogel has good stability under conditions of pH = 3, 7, and 8, its appearance is not easily affected by pH changes. To assess the injectability of the hydrogel we prepared, we loaded the ICG-HPC-AA/BSA hydrogel into a 22 G syringe for injectability testing. As shown in Fig. 3B, we confirmed that the synthesized hydrogel could be injected through the syringe while maintaining its normal form. We also examined the morphology of the ICG-HPC-AA/BSA hydrogel using a scanning electron microscope, and the ICG-HPC-AA/BSA hydrogel exhibited a three-dimensional porous structure (Fig. 3C). We prepared hydrogels with and without rhodamine dye and tested the self-healing property of the hydrogel. In the self-healing test, after cutting the hydrogel and bringing the cut sections into contact, we observed that within 1 min, the incision had healed. Upon stretching, the hydrogel did not fracture. The ICG-HPCAA/BSA hydrogel demonstrated its ability to self-heal without the need for external forces or stimuli. This is attributed to the hydrogel's capacity to reconstruct its gel network through intrinsic molecular interactions, thereby exhibiting excellent self-healing

properties (Fig. 3D and E).

2.8. In vivo degradation detection of ICG-HPC-AA/BSA hydrogel

To study the degradability of the ICG-HPC-AA/BSA hydrogel, considering that direct visual observation of the in vivo degradation of the hydrogel can be clearer and more straightforward, we chose to directly observe the degradation of the hydrogel in the mice. As shown in Fig. 3F, the volume of the hydrogel in the mice gradually decreased over time, and the hydrogel in the body was completely degraded by the 12th day. Moreover, no swelling, ulceration, or other pathological changes were observed around the injection site of the hydrogel. The hydrogel we prepared can degrade and disappear in the mice, has good safety for the mice, and possesses good biocompatibility.

2.9. Near-infrared imaging of hydrogel in vivo

ICG has excellent photothermal properties and fluorescence imaging capabilities. We can not only use near-infrared laser irradiation to promote the ICG-HPC-AA/BSA hydrogel to generate heat, thus achieving the effect of photothermal therapy, but also monitor the presence of the hydrogel in the mice through near-infrared imaging. We used the IVIS spectral imaging system for the near-infrared imaging of the mice. As shown in Fig. 3G, the fluorescence intensity significantly increased within 0–6 h after the hydrogel injection into the mice, peaking between 4 and 6 h, and then the fluorescence intensity gradually decreased. This result indicates that the use of ICG in the hydrogel can achieve in vivo fluorescence imaging with deep tissue penetration.

2.10. Toxicity of G-Rh2 in H22 cells and CT26 cells

Upon co-incubation of H22 cells with 1 mg/mL G-Rh2, the FITC+/PI- ratio for early apoptosis
reached 3.05 % and the FITC+/PI + ratio for late apoptosis reached 11.2 %. In comparison, the NS group showed 0.65 % early and 1.18 % late apoptosis. This difference indicated that G-Rh2 induced both early and late apoptosis in H22 cells (Fig. 4A). As shown in Fig. 6A, we observed that the proportion of early apoptosis (Annexin V-FITC+/PI-) in CT26 cells treated with 1 mg/mL of G-Rh2 reached 19.3 %, and the
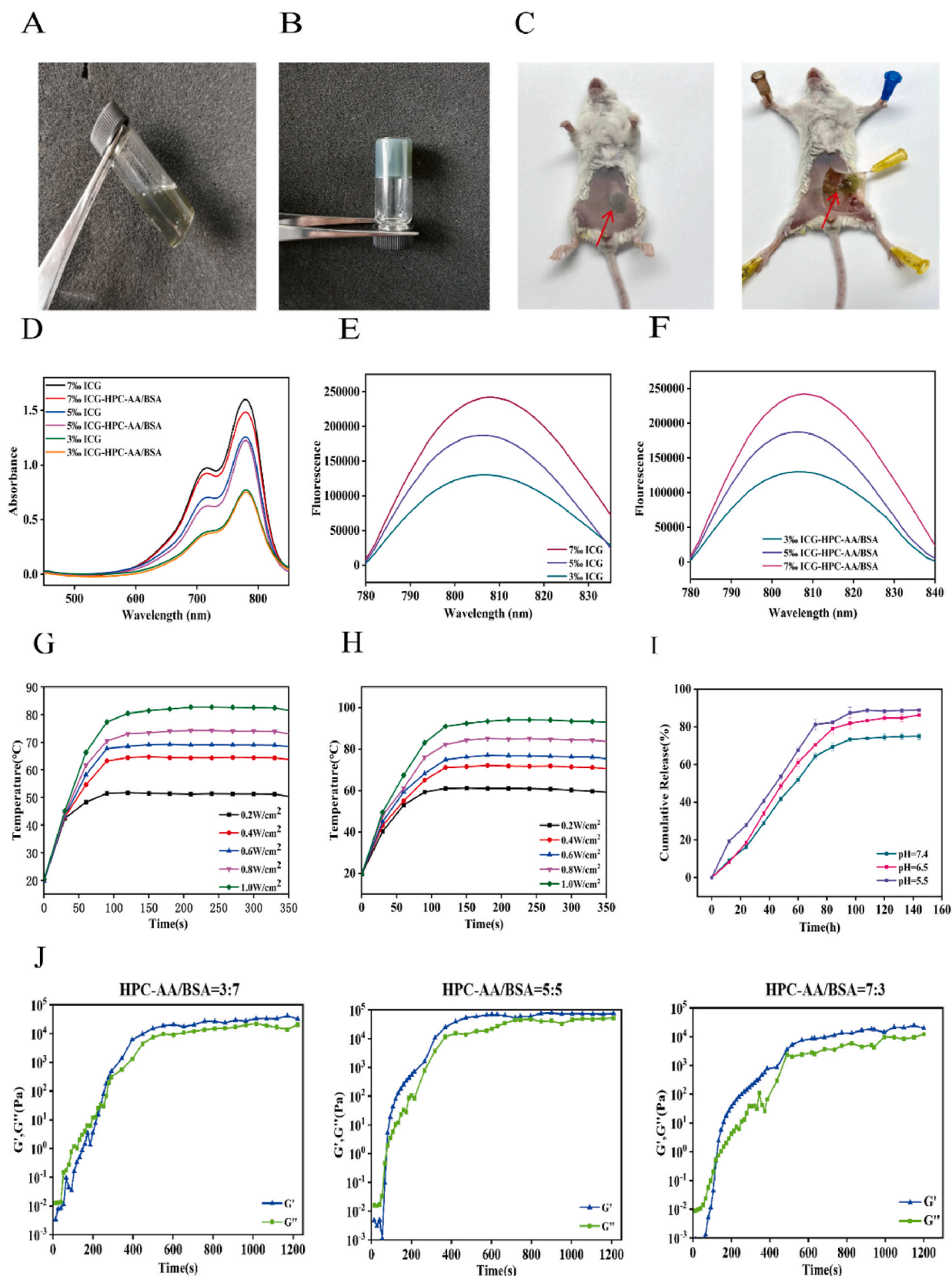
Fig. 2. Characterization of ICG-HPC-AA/BSA hydrogel. (A) Hydrogel state of 5 ‰ ICG-HPC-AA/BSA at 25 °C; (B) Hydrogel state of 5 ‰ ICG-HPC-AA/BSA at 37 °C; (C) Photos of the G-Rh2-loaded hydrogel in mice; (D) NIR-UV-VIS absorption of ICG solution and ICG-HPC-AA/BSA hydrogel; (E) Fluorescence spectra of ICG solution; (F) Fluorescence spectra of ICG-HPC-AA/BSA hydrogel; (G) Photothermal curve of 5 ‰ ICG-HPC-AA/BSA hydrogel; (H) Photothermal curves of 7 ‰ ICG-HPC-AA/BSA hydrogel; (I) In vitro release curve of G-Rh2 in hydrogel; (J) Determination of rheological properties of 5 ‰ ICG-HPC-AA/BSA hydrogel with different proportions.
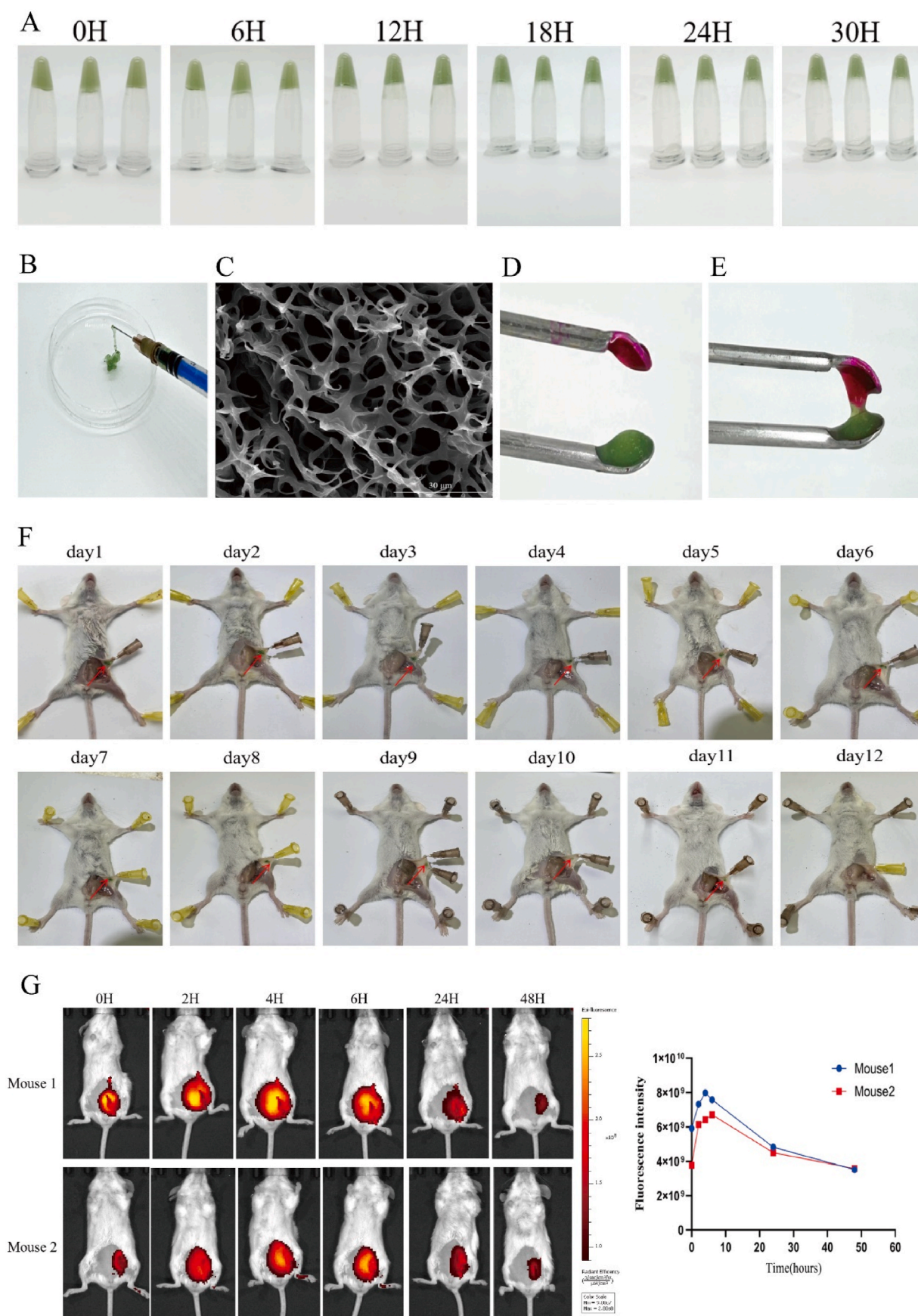
Fig. 3. (A) The stability of the ICG-HPC-AA/BSA hydrogel at different pH values; (B) The injectability of the hydrogel; (C) The scanning electron microscope image of the ICG-HPC-AA/BSA hydrogel; (D–E) Self-healing test of the ICG-HPC-AA/BSA hydrogel; (F) In vivo degradation detection of ICG-HPC-AA/BSA hydrogel; (G) Near-infrared imaging of hydrogels in vivo.
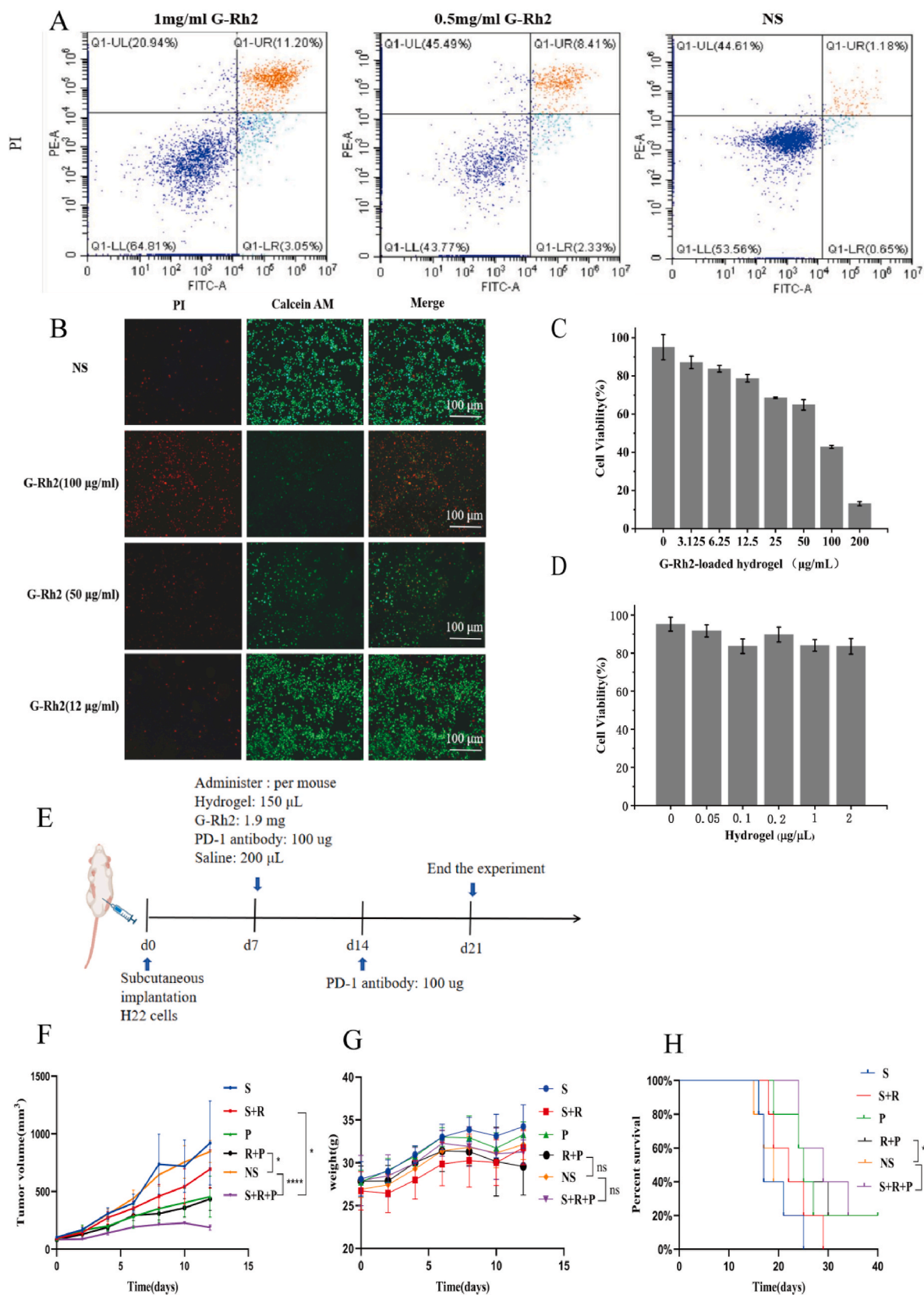
Fig. 4. (A) Detection of apoptosis in H22 cells treated with different G-Rh2 concentrations; (B) Calcein AM and PI staining of H22 cells incubated with G-Rh2; (C) Cell toxicity of G-Rh2-loaded hydrogel on H22 cells; (D) Cell toxicity of different ICG-HPC-AA/BSA hydrogel concentrations on H22 cells; (E) Schematic representation of the therapy experiment in mice with H22 tumors; (F) Inhibition of H22 tumors growth in each treatment group; (G) Changes in weights of mice in each treatment group; (H) Survival curves of mice with H22 tumors in each treatment group.

proportion of late apoptosis (Annexin V-FITC+/PI+) reached 11.1 %. In contrast, the early apoptosis proportion in the NS group was 7.23 %, and the late apoptosis proportion was 1.37 %. This suggested that G-Rh2 promoted both early and late apoptosis in CT26 cells. Fluorescence staining was performed to distinguish between the live and dead H22 cells. Propidium Iodide (PI) staining generated red fluorescence, indicating dead cells, while Calcein AM staining produced green fluorescence, indicating live cells. The fluorescence staining images revealed that the group treated with 100 μg/mL G-Rh2 had the strongest effect on promoting H22 cell death among the tested concentrations (Fig. 4B).

2.11. Toxicity of G-Rh2-loaded hydrogel or hydrogel

The MTT assays demonstrated a decrease in the survival rates of H22 and CT26 cells with increasing concentrations of G-Rh2 in the ICG-HPC-AA/BSA hydrogel (Fig. 4C and 6B). This indicated a concentration-dependent toxic effect of the G-Rh2-loaded hydrogel on both cell lines. As shown in Fig. 6D, survival rates of Human umbilical vein endothelial cells (HUVEC cells) were over 90 % when treated with G-Rh2-loaded hydrogel at concentrations ranging from low (3.125 μg/mL) to high (50 μg/mL). This suggested that G-Rh2-loaded hydrogel had good safety in HUVEC cells. Notably, the survival of both cell lines exceeded 90 % at a concentration of 0.05 μg/μL of the ICG-HPC-AA/BSA hydrogel. Even at the highest concentration of hydrogel (2 μg/μL), the survival rate remained above 80 % (Fig. 4D and 6C). These results highlighted the excellent biocompatibility of the hydrogel and its potential as an effective G-Rh2 delivery system.

2.12. Assessment of antitumor effects in mice with H22 tumors

Compared to the NS (Normal Saline, NS) group, both the S + R + P (Hydrogel + G-Rh2 + PD-1 Monoclonal Antibody, S + R + P) group and the R + P (G-Rh2 + PD-1 Monoclonal Antibody, R + P) group showed significant inhibition of H22 tumor growth. Schematic representation of the therapy experiment in mice with H22 tumors was shown in the figure (Fig. 4E). Notably, the S + R + P group showed the most significant reduction in tumor growth (Fig. 4F and 5A). Additionally, the S + R + P group significantly increased the secretion levels of TNF-α and IFN-γ in mice (Fig. S3), which contributed to the improved antitumor treatment outcomes in mice with H22 tumors. Throughout the observation period, the average body weights of mice in all groups generally increased from their pretreatment weights (Fig. 4G). No significant differences in body weight were observed among the treatment groups.

2.13. Survival analysis of mice with H22 tumors

Compared to the survival rates of mice in the NS group, both the S + R + P and R + P groups exhibited improved survival rates and prolonged survival times (Fig. 4H). Moreover, combination therapy with G-Rh2 and PD-1 antibody not only demonstrated a synergistic antitumor effect but also showed promise in prolonging the survival times of mice with H22 tumors.

2.14. Expression analysis of CD3 and PD-L1 in H22 tumors

Lymphocytes, particularly CD3$^+$ T cells, are crucial for antitumor immunity. G-Rh2 enhances the activity of T lymphocytes by mobilizing them into the tumor microenvironment, thereby inhibiting melanoma growth and extending survival in mice [23]. Song C et al. demonstrated that injectable nanogels can reshape the immunosuppressive tumor microenvironment by controlled release of immunomodulatory agents. This process activates antigen-presenting cells and promotes the generation of antigen-specific T cells [24]. Targeting PD-1 or its ligand, PD-L1, is a key strategy in tumor immunotherapy. Recent findings have indicated that ginsenoside metabolites can inhibit PD-1/PD-L1 interactions, suggesting their potential as novel therapeutic agents [14].

Therefore, we evaluated the expression levels of CD3 and PD-L1 in tumor tissues of the treated group.

Immunofluorescence experiments were conducted on H22 tumor tissues from three distinct groups targeting CD3 and PD-L1. Fluorescence results revealed that the S + R + P and R + P groups exhibited higher CD3 + lymphocyte infiltration, with the most pronounced infiltration observed in the S + R + P group (Fig. 5B). Peritumoral injection of G-Rh2-loaded hydrogel slowed the release of G-Rh2 in tumor tissue and promoted the recruitment of T lymphocytes. According to the analysis of PD-L1 expression in tumor tissues (Fig. 5C), PD-L1 expression of tumor cells in the NS group was higher than that in the S + R + P and R + P groups. This result signifies the heightened antitumor efficacy in these two experimental groups, corresponding to lower PD-L1 expression levels in their tumor tissues.

2.15. Analysis of M1 macrophages in H22 tumors and spleens

Macrophages exhibit two distinct activation states, M1 and M2. M1 macrophages are associated with pro-inflammatory and antitumor responses, whereas M2 macrophages are linked to immunosuppression and tumor immune evasion. The macrophage type can significantly influence the effectiveness of antitumor immunotherapy. G-Rh2 triggers the transformation of M2 to M1 macrophages, enhances their regulation of non-small cell lung cancer, and restricts lung cancer cell migration and invasion [25]. In this study, we examined the effects of G-Rh2-loaded hydrogel and systemic PD-1 monoclonal antibodies on macrophage activation in the tumor microenvironment. We analyzed the proportions of CD11b + F4/80+CD86$^+$ cells, indicating M1 macrophages, in tumor tissues (Fig. 5D and F) and spleens (Fig. 5E and G) using flow cytometry. Comparative assessments revealed that the S + R + P group exhibited the highest distribution of M1 macrophages within the tumor tissues compared to other treatment groups. Importantly, the tumor tissues of the S + R + P group hosted a greater influx of M1 macrophages than those of the NS group, indicating a statistically significant difference. However, the proportion of M1 macrophages within the tumor tissues of the R + P group was not significantly different from that of the NS group. Compared to the NS group, more M1 macrophages infiltrated the spleen in the S + R + P and R + P groups, but there were fewer M1 macrophages in the tumor tissues in the R + P group. This may be due to the recruitment process of splenic M1 macrophages to tumor tissues in the R + P group was regulated by other factors. These results suggested that S + R + P treatment promoted the formation of M1 macrophages both in the tumor and spleen, facilitated the migration of M1 macrophages from the mouse spleen to the tumor tissue, and exerted antitumor effects. Consequently, the S + R + P group demonstrated advantages over the R + P group in terms of anti-H22 tumor treatment.

2.16. Evaluation of antitumor efficacy in mice with CT26 tumors

To investigate whether the combination of G-Rh2-loaded hydrogel and PD-1 antibody exhibits equivalent antitumor therapeutic effects on other types of tumors. We further investigated the impact of the thermo-responsive ICG-HPC-AA/BSA hydrogel combined with G-Rh2 and PD-1 monoclonal antibody on CT26 tumors in mice. Schematic representation of the therapy experiment in mice with CT26 tumors was shown in the figure (Fig. 6E). Compared across groups, the H + S + R + P (808 nm Laser treatment + Hydrogel + G-Rh2 + PD-1 Monoclonal Antibody, H + S + R + P) group significantly inhibited the growth of CT26 tumors, with a statistically significant difference (Fig. 6F). Moreover, the H + S + R + P group increased the serum secretion levels of IL-12p70 and IFN-γ in mice (Fig. S4). Both IL-12p70 and IFN-γ are crucial for their role in antitumor activities. Throughout the observation period, the average body weights of mice in all groups generally increased from their pretreatment weights (Fig. 6G). No significant differences in body weight were observed among the treatment groups.

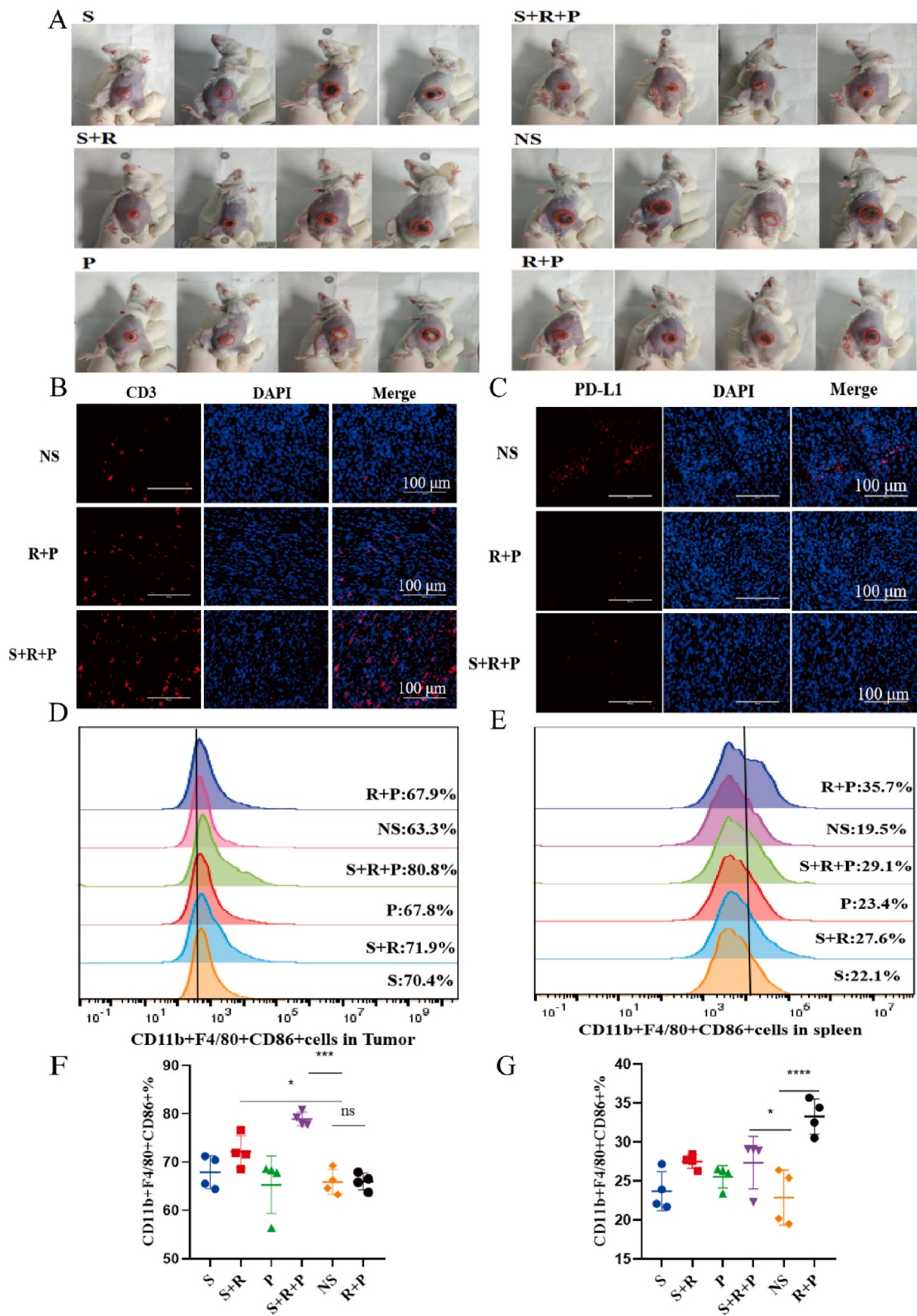**Fig. 5.** (A) Photographs of H22 tumors in mice in each group; (B) Expression of CD3$^+$ lymphocytes in tumor tissues; (C) Expression of PD-L1 in tumor tissues; (D) Typical representation of M1 macrophages in H22 tumors; (E) Typical representation of M1 macrophages in spleens of mice with H22 tumors; (F) The proportion of M1 macrophages in H22 tumors; (G) The proportion of M1 macrophages in spleens of mice with H22 tumors.
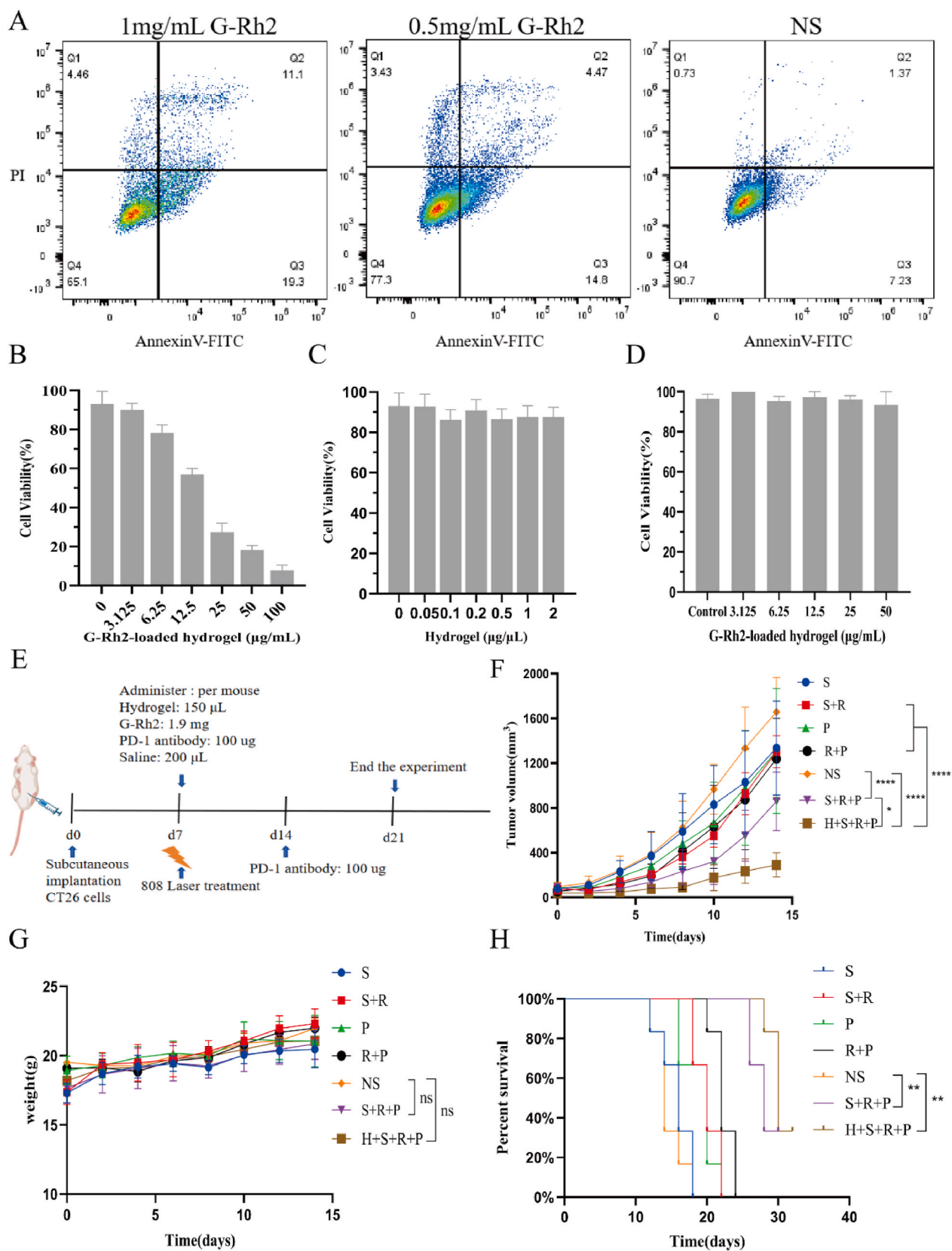
Fig. 6. (A) Detection of apoptosis in CT26 cells treated with different G-Rh2 concentrations; (B) Cell toxicity of G-Rh2-loaded hydrogel on CT26 cells; (C) Cell toxicity of different ICG-HPC-AA/BSA hydrogel concentrations on CT26 cells; (D) Cell toxicity of G-Rh2-loaded hydrogel on HUVEC cells; (E) Schematic representation of the therapy experiment in mice with CT26 tumors; (F) Inhibition of CT26 tumors growth in each treatment group; (G) Changes in weights of mice with CT26 tumors; (H) Survival curves of mice with CT26 tumors in each treatment group.

2.17. Survival analysis of mice with CT26 tumors

Compared to the survival rates of mice in the NS group, both the S + R + P and H + S + R + P groups showed significantly enhanced survival rates and extended survival times in mice with CT26 tumors (Fig. 6H). This suggested that the combination of the thermo-responsive ICG-HPC-AA/BSA hydrogel, G-Rh2, and PD-1 monoclonal antibody could improve the survival times of mice with CT26 tumors.

2.18. Expression analysis of CD3, PD-L1, macrophages in CT26 tumors

Immunofluorescence experiments were conducted on CT26 tumor tissues from three groups (NS, H + S + R + P and S + R + P groups). Among these groups, the H + S + R + P and S + R + P groups exhibited higher CD3 + lymphocytes infiltration (Fig. 7A). *In situ* injection of G-Rh2-loaded hydrogel slowed the release of G-Rh2 in tumor tissue and promoted the recruitment of T lymphocytes. According to the analysis of PD-L1 expression in tumor tissues (Fig. 7B), PD-L1 expression of tumor cells in the NS group was higher than that in the H + S + R + P and S + R + P groups. M1 macrophages in the H + S + R + P and S + R + P groups showed a significant increase compared to that in the NS group (Fig. 7C). In comparison to the NS group, the S + R + P group exhibited lower M2 macrophages in CT26 tumors, while the H + S + R + P group showed the lowest M2 macrophages (Fig. 7D).

2.19. Analysis of M1 and M2 macrophages in mice with CT26 tumors

To determine whether the immunomodulatory effects observed in the S + R + P group were applicable to other tumor types, we conducted additional validation using the CT26 colon cancer model. In this experiment, we administered the G-Rh2-loaded ICG-HPC-AA/BSA hydrogel along with PD-1 antibody treatment and 808 nm laser irradiation (0.3 W, 5 min) to the experimental group, referred to as the H + S + R + P group. Using flow cytometry, we evaluated the infiltration ratios of M1 (CD11b+, F4/80+, and CD86+) and M2 macrophages (CD11b+, F4/80+, and CD163+) in CT26 tumors. Compared to the NS group, the H + S + R + P and S + R + P groups showed a higher proportion of M1 macrophages in the tumor (Fig. 8A and G), indicating the ability to promote M1 macrophages infiltration and foster a favorable antitumor microenvironment in CT26 tumors. Among the groups, the S + R + P groups had a lower proportion of M2 macrophages in the tumor, while the H + S + R + P group had the lowest proportion (Fig. 8B and H). This suggested that the thermal energy generated by the 808 nm laser irradiation of the G-Rh2-loaded hydrogel significantly reduced the infiltration of M2 macrophages in the CT26 tumor microenvironment.

2.20. Analysis of activated dendritic cells in mice with CT26 tumors

Both the S + R + P and H + S + R + P groups showed a significant increase in the proportion of activated CD11c + CD86+ dendritic cells in the spleens of mice compared to the NS group (Fig. 8C and I). These activated dendritic cells are essential for presenting tumor antigens, which are crucial for lymphocytes to recognize and initiate antitumor immune responses. This increase indicates the favorable antitumor therapeutic effects of the groups and suggests their potential to enhance antitumor immunity.

2.21. Analysis of memory T cells in mice with CT26 tumors

Memory T cells and effector memory T cells play crucial roles in antitumor therapy by providing long-lasting immune surveillance and rapid response to tumor re-emergence. Therefore, we analyzed memory T cells within the lymph nodes and spleens of mice and distinguished between central memory T cells (T_{CM}: $CD3^+CD8^+CD44+CD62L+$) and effector memory T cells (T_{EM}: $CD3^+CD8^+CD44+CD62L-$) using flow cytometry. Both the H + S + R + P and S + R + P groups exhibited

elevated $CD8^+$ T cells proportions in CT26 tumors compared to the NS group (Fig. 8D and J). The H + S + R + P group demonstrated the highest proportion of T_{CM} within the draining lymph nodes (Fig. 8E and K), and both the H + S + R + P and S + R + P groups exhibited elevated T_{EM} proportions within the draining lymph nodes compared to the NS group (Fig. 8E and L). The S + R + P group displayed a higher proportion of T_{EM} within the spleens than the NS group (Fig. 8F and M), whereas this distinction between the H + S + R + P and NS groups did not reach statistical significance. This outcome could potentially be attributed to the greater migration of intrasplenic T_{EM} to the draining lymph nodes, where they exert their antitumor effects in the H + S + R + P group. These findings underscore the capacity of combination treatment strategies to activate T lymphocytes and enhance the efficacy of antitumor immunotherapy.

2.22. RNA sequencing results from mice with CT26 tumors

Subsequently, we conducted RNA transcriptome sequencing of CT26 tumor tissues from mice in the H + S + R + P, S + R + P, and NS treatment groups. Signal pathway enrichment analysis of the differentially expressed genes using KEGG revealed significant findings. In the flow cytometry experiments, we observed a significant upregulation of immune cell subsets in the H + S + R + P group, including M1 macrophages, effector T cells, memory T cells, and dendritic cells. The transcriptome sequencing results of the H + S + R + P group compared to the NS group showed significant enrichment in multiple immune signaling pathways. These pathways included cytokine-cytokine receptor interactions, chemokine signaling pathways, regulation of stem cell pluripotency, Th1 and Th2 cell differentiation, and B cell receptor signaling pathways (Fig. 9A). Specifically, upregulations of cytokine-cytokine receptor interactions and chemokine signaling pathways are crucial for immune cells recruitment and activation, facilitating deep infiltration of T lymphocytes into tumor tissues [26,27]. Moreover, the upregulation of pathways regulating stem cell pluripotency suggests potential roles in modulatng immune cell states within the tumor microenvironment, essential for immune cells differentiation and function [28]. The enhancement of Th1 and Th2 cell differentiation and B cell receptor signaling pathways further supports activation of the adaptive immune response, consistent with the observed upregulation of effector and memory T cells by flow cytometry, indicating improved adaptive immune response. An immune gene heatmap analysis (Fig. 9B) revealed significant enrichment of genes such as *Iigp1, Nlrc5, Nlrc4, Casp8, Iigp1, Cd4* and *Ifnlr1* in the H + S + R + P group compared to the NS group. These genes are involved in immune regulation, cytokine production, and antigen presentation, crucial for activating the tumor immune microenvironment. For instance, *Nlrc5*, known for its role in regulating MHC class I molecule expression and antigen presentation, plays a critical role in recruiting and activating tumoricidal $CD8^+$ T cells in human cancer immunity [29]. Furthermore, the volcano plot comparing H + S + R + P and NS groups (Fig. 9E) highlighted significant regulation of genes such as *Runx3* in the H + S + R + P group, with *Runx3* associated with tumor suppression [30]. Meanwhile, the S + R + P group exhibited upregulation of immune signaling pathways such as cytokine-cytokine receptor interactions, chemokine signaling pathways, IL-17 signaling pathway, and antigen processing and presentation. Immunogene heat maps and volcano plots revealed significant enrichment of genes such as *Ccl7* and *Ifi44* in the S + R + P group compared to the NS group (Fig. S5). For example, *Ccl7* upregulates JAK2/STAT1 protein levels in macrophages, promoting polarization towards the M1 phenotype [31].

Furthermore, the H + S + R + P group showed higher activity than the S + R + P group in other immune signaling pathways such as cytokine-cytokine receptor interactions, cell adhesion molecules, and regulation of stem cell pluripotency (Fig. 9C). In particular, upregulation of cell adhesion molecules may be related to the positioning and interaction of immune cells [32]. This also indicates that laser irradiation
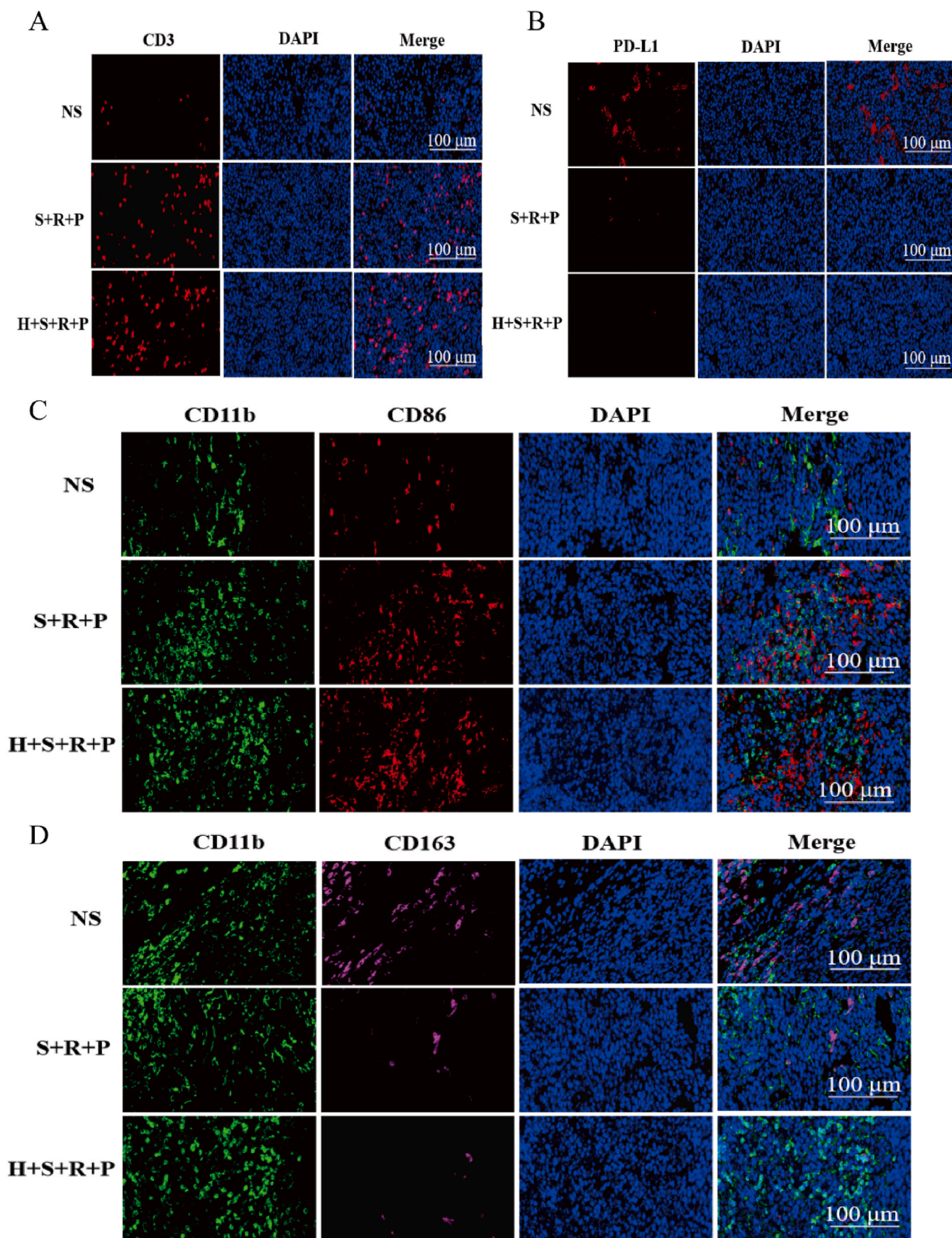
Fig. 7. (A) Expression of CD3^{+} lymphocytes in CT26 tumor tissues; (B) Expression of PD-L1 in CT26 tumor tissues; (C) Expression of M1 macrophages in CT26 tumor tissues; (D) Expression of M2 macrophages in CT26 tumor tissues.
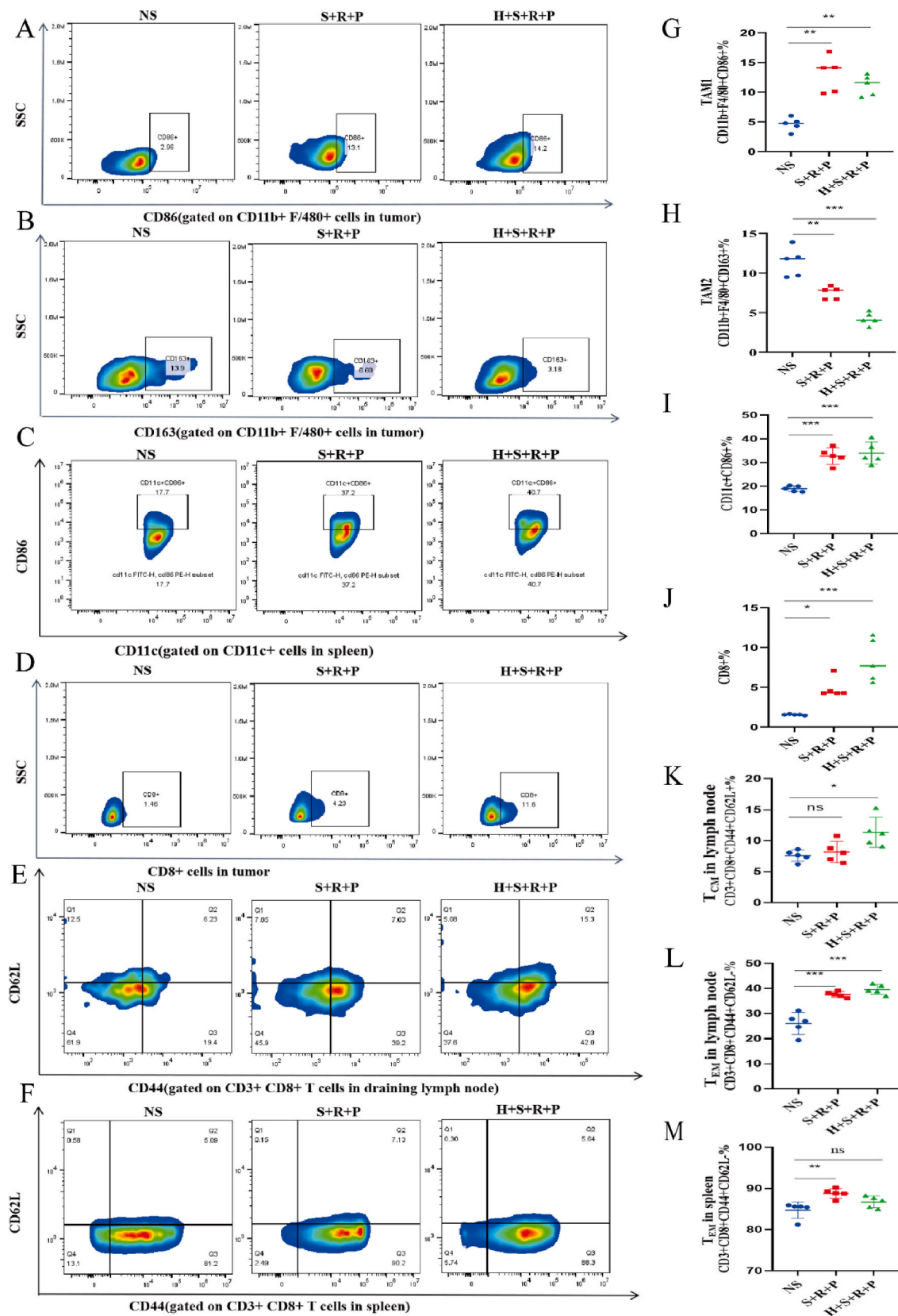
Fig. 8. (A) Typical images of M1 macrophages in CT26 tumors; (B) Typical images of M2 macrophages in CT26 tumors; (C) Typical images of activated dendritic cells in spleens; (D) Typical images of CD8+T lymphocytes in CT26 tumors; (E) Typical images of T_{CM} cells and T_{EM} cells of draining lymph nodes; (F) Typical images of T_{EM} cells of spleens; (G) The proportion of M1 macrophages in CT26 tumors; (H) The proportion of M2 macrophages in CT26 tumors; (I) The proportion of activated dendritic cells in the spleens; (J) The proportion of CD8+T lymphocytes in CT26 tumors; (K) The proportion of T_{CM} cells in draining lymph nodes; (L) The proportion of T_{EM} cells in draining lymph nodes; (M) The proportion of T_{EM} cells in spleens.
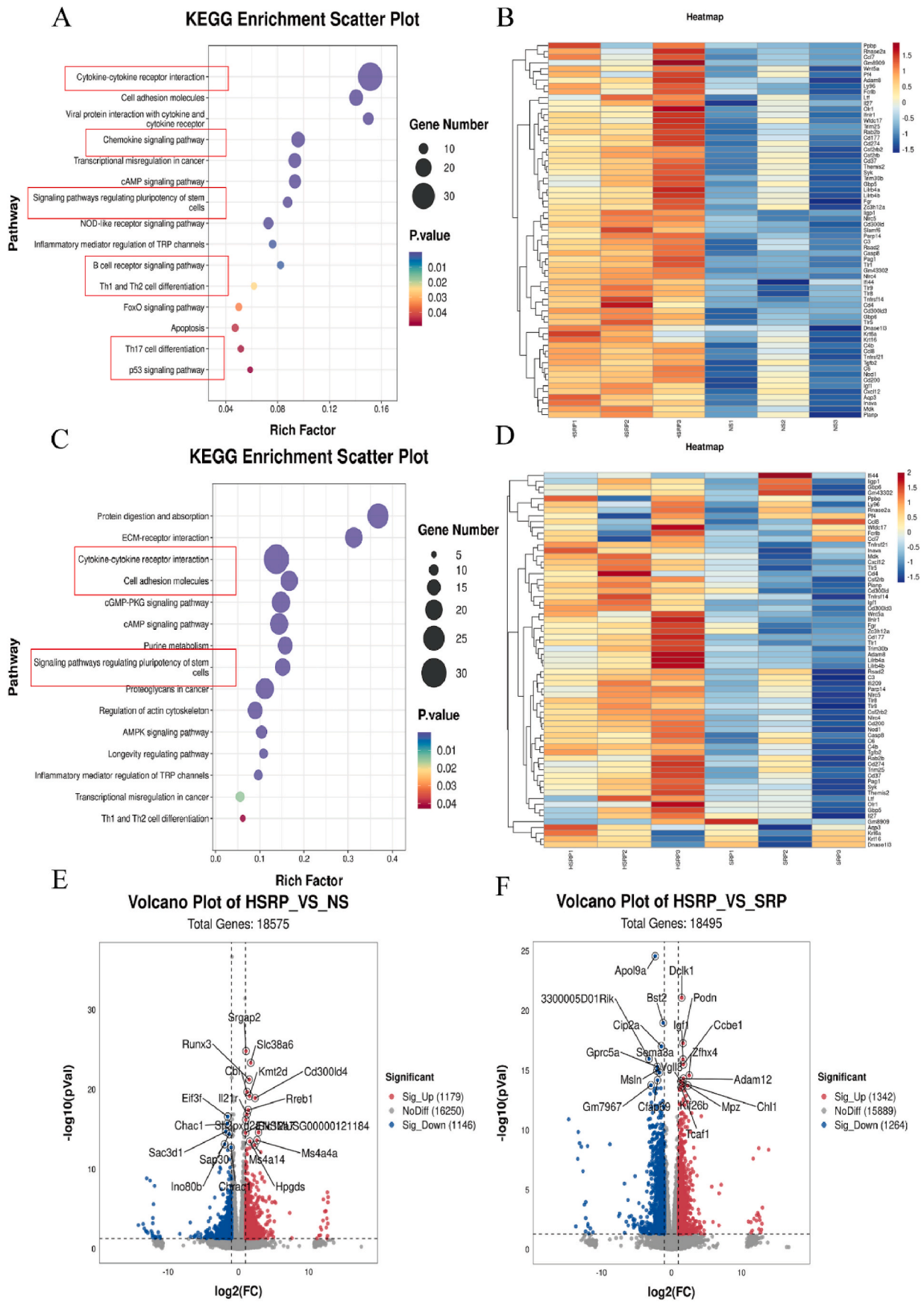
Fig. 9. (A) HSRP VS NS up-regulated Kegg enrichment factor map; (B) Immune gene heat map of HSRP and NS; (C) HSRP VS SRP up-regulated Kegg enrichment factor map; (D) Immune gene heat map of HSRP VS SRP; (E) Differential gene volcano map of HSRP VS NS; (F) Differential gene volcano map of HSRP VS SRP.

helps further activate immune cells in the tumor microenvironment. Comparing the immune gene heatmap of the H + S + R + P group with that of the S + R + P group (Fig. 9D), genes such as *Tnfrsf21*, *Cxcl12*, *Tlr5*, and *Csf2rb* were significantly enriched in the H + S + R + P group. According to the literature reports, *Tnfrsf21* acts as a tumor development suppressor by promoting necroptosis, and patients with high expression of *Tnfrsf21* have a relatively higher survival rate [33]. The volcano plot (Fig. 9F) revealed that the H + S + R + P group exhibited upregulation of genes related to tumor suppression, gene transcription, and cell migration, such as *Ccbe1, Zfhx4,* and *Sema3a,* compared to the S + R + P group.

In summary, both the H + S + R + P and S + R + P treatment groups demonstrated significant upregulation of immune signaling pathways and immune-related genes expression, enhancing the antitumor capabilities in CT26 colon cancer mouse models. These sequencing findings align with the observed upregulation of various immune cell subsets in flow cytometry experiments, indicating a highly active immune response environment characterized by coordinated actions of diverse immune cell types and signaling pathways in these groups. These results offer new insights into understanding immune cell subsets' roles in antitumor immune responses and may guide the development of intervention strategies targeting specific immune pathways.

2.23. Histopathological analysis of tissues under various treatments

Hematoxylin and eosin (HE) staining was conducted to evaluate potential pathological changes in the heart, liver, spleen, lungs, and kidneys tissues of mice from each treatment group. The examination showed no significant pathological alterations across these tissues among the different treatment groups, and the tissue morphology remained consistent in eac h group (Fig. S6, Fig. S7). Similar to the NS group, the HE staining results from the other treatment groups indicated no adverse effects. This finding indicated that the treatments, including G-Rh2, ICG-HPC-AA/BSA hydrogel, and PD-1 monoclonal antibody, did not induce serious adverse reactions in mice. This suggested that these treatment schemes did not damage vital organs, indicating good biosafety for mice.

3. Conclusion

In this study, we designed and synthesized a novel *in situ* vaccine system using a G-Rh2-loaded hydrogel for treating liver and colon cancers in mice. Our "*in situ* vaccine" approach involved localized delivery of an ICG-HPC-AA/BSA hydrogel loaded with G-Rh2, ensuring precise and gradual release of G-Rh2 within the tumor environment. This strategy effectively limited drug dispersion beyond the tumor, elicited an immune response, mitigated potential adverse effects on normal abdominal organs, and enhanced the antitumor efficacy of G-Rh2. The three-dimensional porous structure of the ICG-HPC-AA/BSA hydrogel provided dual benefits, it enhanced G-Rh2 encapsulation efficiency and promoted the recruitment of immunomodulatory cells, thereby improving antitumor immunity. Beyond direct tumor inhibition, this *in situ* vaccine also activated tumor autoantigens, boosting the antitumor immune response, especially when combined with systemic PD-1 monoclonal antibody administration. The combination of G-Rh2-loaded ICG-HPC-AA/BSA hydrogel and PD-1 monoclonal antibody significantly enhanced therapeutic outcomes against liver and colon cancers in the mice model. This combination therapy effectively potentiated the immune response against H22 liver cancer and CT26 colon cancer, inhibiting tumor progression and enhancing immune cells infiltration into the tumor microenvironment.

In conclusion, this biocompatible drug delivery system, based on G-Rh2-loaded hydrogel *in situ* vaccine, has the potential to induce robust antitumoral immune reactions, which can be further augmented by PD-1 mAb. This strategy effectively harnesses immune cell infiltration within the tumor milieu while minimising side effects. These promising results

warrant further comprehensive investigations and may eventually pave the way for future clinical applications.

4. Materials and methods

4.1. Materials

Cell culture medium and supplements were purchased from Gibco (NY, USA). Indocyanine green carboxylic acid (ICG-COOH), Bovine serum albumin (BSA), Hydroxypropyl cellulose (HPC) were purchased from Macklin (Shanghai, China). Abietic acid (AA) were purchased from Sigma-Aldrich Company (USA). Ginsenoside Rh2 (G-Rh2) reagents were purchased from Yuanye Biology Company (Shanghai, China). Murine PD-1 monoclonal antibody was purchased from Junmeng Biopharmaceutical Technology Company (Suzhou, China). Mouse CD11b, CD11c, F4/80, CD86, CD163, CD3, CD8, CD44, CD62L and PD-L1antibodies were purchased from Biolegend (CA, USA).

H22 hepatocellular carcinoma cells and CT26 colon cancer cells were obtained from the Cell Bank of Shanghai Institute of Biochemistry and Cell Biology, and cultured with RPMI 1640 medium containing 10 % FBS and 1 % P/S at 37 °C and 5 % CO_2. BALB/c and ICR female mice aged 5–6 weeks were purchased from Shanghai Sippr-BK laboratory animal Co. Ltd. (Shanghai, China) and all procedures were conducted in accordance with the guidelines set by the Experimental Animal Ethics Committee of Nanjing Drum Tower Hospital, the affiliated hospital of Nanjing University Medical School, the animal ethics approval number was 2022AE01011.

4.2. Preparation of ICG-HPC-AA/BSA hydrogel and gel formation time detection

The ICG-HPC-AA/BSA hydrogel was synthesized by dissolving BSA and ICG-HPC-AA in deionized water, resulting in separate solutions with 20 % mass fractions of BSA and ICG-HPC-AA. These solutions were then mixed at various ratios under a temperature of 37 °C, with the addition of HCL solution to achieve the desired pH level in the mixture. Consequently, different ratios of the injectable ICG-HPC-AA/BSA hydrogels were generated. Specifically, ICG-HPC-AA/BSA hydrogels with ratios of 3:7, 5:5, and 7:3 were synthesized. By mixing 20 % concentration ICG-HPC-AA solution and 20 % concentration BSA solution and maintaining a temperature of 37 °C, the gel formation time was determined using the tube inversion method. After mixing ICG-HPC-AA/BSA hydrogels at different ratios (3:7, 5:5, and 7:3), the tube was inverted to determine whether the mixture flowed. When the mixing solution did not flow, the sample successfully transitioned from the liquid to the gel state, and the moment at which gel formation occurred was recorded.

4.3. Photothermal performance test of the ICG-HPC-AA/BSA hydrogel

The photothermal properties of the ICG solution and ICG-HPC-AA/BSA hydrogels were examined by UV absorption and fluorescence spectral analyses. ICG solutions of varying concentrations (3, 5, and 7 ‰) and ICG-HPC-AA/BSA hydrogels with different ICG-COOH contents (3, 5, and 7 ‰) were prepared. UV–visible spectrophotometry was used to measure the ultraviolet absorption spectra of each group, whereas the fluorescence spectra of each group were measured using a fluorescence spectrometer under 808 nm laser excitation. The photothermal capabilities of the ICG-HPC-AA/BSA hydrogel and other materials were evaluated using thermal imaging technology in conjunction with an 808 nm laser.

4.4. Rheological characterization of the 5 ‰ ICG-HPC-G-AA/BSA hydrogel

A DHR-I rheometer (TA Instruments, Italy) equipped with parallel plate geometry (diameter = 40 mm) was used for rheological testing.

The rheological experiment aimed to assess the stability of the 5‰ICG-HPC-G-AA/BSA hydrogel, which was achieved through a time-scanning shaking experiment.

4.5. In vitro release of ICG-HPC-AA/BSA hydrogel loaded with G-Rh2

During the preparation of the ICG-HPC-AA/BSA hydrogel, a 1 % mass fraction of the G-Rh2 solution was added to obtain an injectable thermal-responsive responsive hydrogel. The G-Rh2-loaded hydrogel was sealed in a dialysis bag with a 10,000 Da molecular weight cutoff and immersed in 500 mL of buffer at pH 5.5, 6.5, and 7.4. At regular time intervals, 1 mL of the buffer was sampled and immediately replenished with an equal volume of fresh buffer to enable the collection of the released G-Rh2. The amount of G-Rh2 released at various time points was determined by UV spectrophotometry.

4.6. Gelled photograph of ICG-HPC-AA/BSA hydrogel

After preparing the ICG-HPC-AA/BSA hydrogel, gel formation experiments were conducted in vitro at temperatures of 25 °C and 37 °C. For in vivo application, the liquid ICG-HPC-AA/BSA hydrogel (0.15 mL, pH 5.6) containing 1.9 mg of G-Rh2 was injected into mice. Post-injection, the hydrogel was heated for 2 min using a 40 °C heating device to induce gelation. The final state of the hydrogel was photographed.

4.7. Performance test of ICG-HPC-AA/BSA hydrogel

To evaluate the stability of the ICG-HPC-AA/BSA hydrogel, we added 100 μL of hydrogel liquid into three 1.5 mL EP tubes, heated them in a 37 °C water bath for 5 min, after which the hydrogel liquid transitioned from a solution to a gel state. Then, we added 1 mL of PBS solution with pH values of 3, 7, and 8 into the EP tubes, respectively. These tubes were maintained in a continuously heated environment at 37 °C water bath, and photographs were taken every 6 h to observe changes in the appearance of the hydrogel. To evaluate the injectability of the prepared hydrogel, we used a single-needle injection system. The synthesized hydrogel was aspirated into a 22 G syringe, and the hydrogel was expelled through the syringe to observe its injectability. The ICG-HPC-AA/BSA hydrogel sample was frozen and then dried to remove moisture and prevent structural collapse. By adjusting the focus and magnification of the scanning electron microscope, a clear image of the hydrogel was obtained. Self-healing hydrogel can shorten the gelation time and promote their application of *in situ* gel systems. They also contribute to the high retention characteristics at the injection site. The self-healing ability of the ICG-HPC-AA/BSA hydrogel was studied through tensile tests. Hydrogels with or without rhodamine dye were prepared, subsequently tested for their self-healing properties after attachment.

4.8. In vivo degradation detection of ICG-HPC-AA/BSA hydrogel

To investigate the degradation performance of the ICG-HPC-AA/BSA hydrogel in mice, we selected 5-week-old female Balb/c mice and subcutaneously injected 150 μL of the hydrogel, ensuring that the initial amount of hydrogel injected into each mouse was consistent. We euthanize one mouse at the same time every day, dissected the area where the hydrogel was injected, observed the degradation of the hydrogel and the morphology of the surrounding skin tissue, and recorded the observations through photography.

4.9. Near-infrared imaging of hydrogel in vivo

To verify that the ICG-HPC-AA/BSA hydrogel can achieve the effect of in vivo observation, we added a near-infrared I-region fluorescent dye, ICG, during the synthesis of the hydrogel. We used an IVIS spectral imaging system for near-infrared imaging and selected 5-week-old female Balb/c mice, injecting 150 μL of ICG-HPC-AA/BSA hydrogel subcutaneously. After anesthetizing the mice with isoflurane, near-infrared imaging was performed at various time points using the imaging instrument, 0H, 2H, 4H, 6H, 24H, and 48H, with the signal wavelength collected at Excitation/Emission = 785nm/810 nm.

4.10. Evaluation of G-Rh2 toxicity on H22 cells and CT26 cells

Apoptoses in H22 cells and CT26 cells were evaluated using the Annexin V-FITC/PI assay. The cells were treated with G-Rh2 at three concentrations (0, 0.5, and 1 mg/mL) in triplicates. After collecting 1×10^5 cells, they were washed twice with precooled saline and centrifuged at $300 \times g$ for 5 min at 4 °C to remove the saline. The cells were then resuspended in 100 μL of $1 \times$ Binding Buffer. Annexin V-FITC (5 μL) and PI Staining Solution (10 μL) were added to the resuspended cells, which were gently mixed and incubated at room temperature in the dark for 15 min. After incubation, the mixture was diluted with 400 μL of $1 \times$ Binding Buffer and kept on ice. The prepared samples were analyzed within 1 h using a flow cytometer.

Calcein AM and PI staining assays were performed to assess the viability of H22 cells treated with G-Rh2. The H22 cell suspensions were plated at a density of approximately 1×10^4 cells per well in a 96-well plate. The cells were exposed to different concentrations of G-Rh2 (12, 50, and 100 μg/mL), along with NS group. Each concentration group consisted of three parallel wells. After a 24-h incubation period, the cells were centrifuged at $250 \times g$ for 5 min at room temperature and washed with PBS. The cells were stained with Calcein AM and PI in each well and incubated in the dark at 37 °C for 30 min. After incubation, the fluorescence of the stained cells was observed under a fluorescence microscope to evaluate cell viability.

4.11. Toxicity of G-Rh2-loaded ICG-HPC-AA/BSA hydrogel to different cells

MTT assays were conducted to evaluate the viability of H22 cells and CT26 cells treated with the ICG-HPC-AA/BSA hydrogel containing various concentrations of G-Rh2. Cells were seeded at a density of 3000 cells per well in 96-well plates and cultured at 37 °C in a 5 % CO$_2$ atmosphere for 24 h. The cells were then exposed to the hydrogel with increasing concentrations of G-Rh2 (0, 3.125, 6.25, 12.5, 25, 50, 100, and 200 μg/mL). After 24-h incubation with the hydrogel, MTT assays were used to assess cells viability. HUVEC cells were cultured in a 96-well plate (5000 cells per well) for 24 h, and then exposed to HUVEC-specific culture medium containing different concentrations of G-Rh2-loaded hydrogel, with the G-Rh2 at concentrations of 0, 3.125, 6.25, 12.5, 25, and 50 μg/mL. After incubation at 37 °C for 24 h, the cells were washed with PBS solution, and CCK-8 reagents were added to each well, followed by incubation at 37 °C in the dark for 2 h. Subsequently, the optical densities (OD) of each well were measured at a wavelength of 450 nm using a microplate reader.

4.12. Toxicity of hydrogel on H22 cells and CT26 cells

MTT assays were used to assess the safety of the ICG-HPC-AA/BSA hydrogel in H22 cells and CT26 cells. Approximately 3000 cells per well were seeded in a 96-well plate and incubated for 24 h. Subsequently, the cells were grouped according to different concentrations of ICG-HPC-AA/BSA hydrogel components (0, 0.05, 0.1, 0.5, 1, and 2 μg/μL) and incubated for another 24 h. Following incubation, MTT assays were used to assess cells viability. These assays were performed by measuring optical density (OD) at 570 nm using an automated microplate reader. The OD values were used to plot survival curves.

4.13. Effect of treatments on H22 tumors growth

A subcutaneous transplantation tumor model of H22 liver cancer was established using 6-week-old ICR mice. Each of the mice was subcutaneously injected with approximately 2×10^6 H22 cells, with 5 mice per group. When the tumor volume of the mice reached approximately 75 mm^3, they were randomly assigned to six distinct treatment groups. The treatment protocols for each group were as follows.

(1) Hydrogel Group (S): Peritumoral injection of 0.15 mL ICG-HPC-AA/BSA hydrogel solution.
(2) Hydrogel + G-Rh2 Group (S + R): Peritumoral injection of 0.15 mL ICG-HPC-AA/BSA hydrogel solution loaded with 1.9 mg G-Rh2 [34].
(3) PD-1 Monoclonal Antibody Group (P): systemic treatment of 200 μg [35] murine PD-1 monoclonal antibody.
(4) Hydrogel + G-Rh2 + PD-1 Monoclonal Antibody Group (S + R + P): Peritumoral injection of 0.15 mL ICG-HPC-AA/BSA hydrogel solution loaded with 1.9 mg G-Rh2, combined with systemic treatment of 200 μg murine PD-1 monoclonal antibody.
(5) Normal Saline Group (NS): Intraperitoneal injection of 200 μL normal saline.
(6) G-Rh2 + PD-1 Monoclonal Antibody Group (R + P): Intraperitoneal injection of 1.9 mg G-Rh2, coupled with 200 μg murine PD-1 monoclonal antibody.

The dimensions of tumors were directly measured using a vernier caliper, and the weights of the mice were recorded using a weight scale. The tumor volume and weight were assessed every other day. The formula used to calculate tumor volume was $V = A \times B^2/2$, where A represents the longest diameter of the tumor and B denotes the maximum transverse diameter of the tumor.

4.14. Survival analysis of mice with H22 tumors

To establish a subcutaneous transplantation tumor model of H22 liver cancer, approximately 2×10^6 H22 cells were subcutaneously injected into 6-week-old ICR mice. Thirty mice were used, with five mice allocated to each experimental group. When the tumor volume of the mice reached approximately 75 mm^3, they were randomly divided into six treatment groups: hydrogel group (S), hydrogel + G-Rh2 group (S + R), PD-1 monoclonal antibody group (P), hydrogel + G-Rh2 + systemic treatment with PD-1 monoclonal antibody group (S + R + P), normal saline group (NS), and intraperitoneal injection of G-Rh2 + PD-1 monoclonal antibody group (R + P). The survival of the mice was observed once daily for 40 days. Subsequently, survival curves of the mice in each group were constructed using GraphPad Prism 8.

4.15. Immunofluorescence expression of CD3, PD-L1, M1 and M2 macrophages in tumors

Mouse tumor samples from the tumor suppression experiment were processed for section and immunofluorescence staining with CD3, PD-L1, M1 and M2 macrophages. The tissue sections were allowed to reach room temperature for 10 min, after which they were subjected to deparaffinization and hydration. After fixing the sections using a citric acid antigen-repairing solution and a microwave oven for antigen repair, a water-blocking ring was drawn and sealed with BSA. The sections were then incubated with primary and secondary antibodies. DAPI was used to stain the nuclear and resin sealed sections. Images were captured using a fluorescence microscope, and further analyses were performed using the ImageJ software.

4.16. Effects of various treatments on CT26 tumors

A subcutaneous transplantation tumor model of colon cancer was established in 6-week-old BALB/c mice. Subsequently, 2×10^6 CT26 colon cancer cells were subcutaneously injected into each mouse. After 5-day period of tumor formation, the mice were randomly divided into six distinct groups. The treatment methods for each group were as follows: ICG-HPC-AA/BSA hydrogel group (S), Hydrogel + G-Rh2 Group (S + R), PD-1 Monoclonal Antibody Group (P), G-Rh2 + PD-1 Monoclonal Antibody Group (R + P), Hydrogel + G-Rh2 + PD-1 Monoclonal Antibody Group (S + R + P), Normal Saline Group (NS), and 808 nm laser treatment + Hydrogel + G-Rh2 + PD-1 Monoclonal Antibody Group (H + S + R + P). The size of the mouse CT26 tumors was measured using a Vernier caliper and the tumor diameter was assessed every other day. Mouse weight was measured using a weight scale.

The treatment protocols for each group were as follows.

(1) Hydrogels Group (S): Peritumoral injection of 0.15 mL ICG-HPC-AA/BSA hydrogel solution.
(2) Hydrogel + G-Rh2 Group (S + R): Peritumoral injection of 0.15 mL ICG-HPC-AA/BSA hydrogel solution loaded with 1.9 mg G-Rh2 [34].
(3) PD-1 Monoclonal Antibody Group (P): systemic treatment of 200 μg [35] murine PD-1 monoclonal antibody.
(4) Hydrogel + G-Rh2 + PD-1 Monoclonal Antibody Group (S + R + P): Peritumoral injection of 0.15 mL ICG-HPC-AA/BSA hydrogel solution loaded with 1.9 mg G-Rh2, combined with systemic treatment of 200 μg murine PD-1 monoclonal antibody.
(5) Normal Saline Group (NS): Intraperitoneal injection of 200 μL normal saline.
(6) G-Rh2 + PD-1 Monoclonal Antibody Group (R + P): Intraperitoneal injection of 1.9 mg G-Rh2, coupled with 200 μg murine PD-1 monoclonal antibody.
(7) 808 nm laser treatment + Hydrogel + G-Rh2 + PD-1 Monoclonal Antibody Group (H + S + R + P): laser irradiation of 808 nm at 0.3 W cm^{-2} for 5 min irradiation [36], peritumoral injection of 0.15 mL ICG-HPC-AA/BSA hydrogel solution loaded with 1.9 mg G-Rh2, combined with systemic treatment of 200 μg murine PD-1 monoclonal antibody.

4.17. Survival analyses of mice with CT26 tumors

Colon models were established in 6-week-old BALB/c mice via subcutaneous injection of 2×10^6 CT26 tumor cells. Five days after tumor development, the mice were randomly divided into the following treatment groups, S, S + R, P, R + P, S + R + P, NS, and H + S + R + P. The survival of the mice was monitored daily for 40 days. Survival curves of mice were generated using GraphPad Prism 8.

4.18. Analyses of immune cells infiltration by flow cytometry

Flow cytometry was used to evaluate immune cells infiltration in tumor tissues, draining lymph nodes, and spleens of the mice. Tissue samples from each group were processed as follows. Tumor tissues were digested with type IV collagenase and the digestion was terminated with complete culture medium. Directly grind the lymph nodes and centrifuge to obtain lymphocytes. Spleens were treated to lyse the red blood cells. The tissue fragments were filtered through a cell strainer and centrifuged at $300 \times g$ for 5 min. The supernatant was discarded, leaving approximately 1×10^6 cells, which were washed with $1 \times$ PBS. The cells were stained with relevant immune cell antibodies at 4 °C in the dark for 30 min. After staining, the cells were washed, centrifuged, and the supernatant was discarded, leaving an approximate volume of 60 μL in each tube. Immune cells were collected using Beckman instruments and analyzed using FlowJo X software. The gating strategy for immune cells analysis by flow cytometry was illustrated in Fig. S10.

4.19. RNA sequencing method for mouse CT26 tumor tissues

Tumor tissue samples were collected from the H + S + R + P, S + R + P, and NS groups. Freezable tubes were prepared for sample storage, and the sample information was marked on the outer walls and lids of the tubes using an oil-based marker. After the tumor tissue was removed, unnecessary tissue was immediately removed. These samples were transferred to the pre-prepared freezer tubes by tweezers, rapidly cooled in liquid nitrogen, and stored in a refrigerator at −80 °C. Library construction and RNA sequencing were conducted by LCBIOTECHNOLOGIES Co., Ltd. (Hangzhou, China). Transcriptome sequencing involves RNA extraction, assessment of RNA sample quality, library preparation, library purification, library detection, library quantification, cluster generation for sequencing, and computerized sequencing. Rigorous quality control measures were implemented at each experimental stage. Following successful testing, distinct libraries were amalgamated based on criteria such as the effective concentration and desired data volume. Next, Illumina sequencing was performed.

4.20. Biosafety assessments of various treatment groups

The heart, liver, spleen, lungs, and kidneys samples were collected from each treatment group. Tissues were fixed in 10 % neutral formalin for 36 h. After fixation, tissues were washed with PBS and dehydrated using a graded series of ethanol concentrations, followed by transparency with xylene. Tissues were embedded in paraffin after gentle heating. Sections of the paraffin-embedded tissue, approximately 4–5 μm thick, were cut using a rotary microtome. Dewaxing and rehydration were performed, followed by hematoxylin and eosin (HE). The stained sections were mounted with neutral gum for preservation.

5. Statistical analysis

Statistical analyses were performed using GraphPad Prism 8.0.2 statistical software. All results were expressed as $\bar{\text{X}} \pm \text{SEM}$. P value was calculated by two-tailed unpaired t-test or ANOVA. $P < 0.05$ meant that the difference was statistically significant (ns $P > 0.05$, *$P < 0.05$, **$P < 0.01$, ***$P < 0.001$, ****$P < 0.0001$). Flow data were analyzed using FlowJo X software. Graphics were drawn using Adobe Illustrator or ImageJ software.

CRediT authorship contribution statement

Chunhua Li: Writing – original draft, Visualization, Validation, Methodology, Data curation, Conceptualization. **Dan Lei:** Visualization, Validation. **Yudong Huang:** Visualization, Validation. **Yuanhao Jing:** Validation. **Wanru Wang:** Investigation. **Lanqi Cen:** Visualization. **Zijian Wei:** Data curation. **Anni Chen:** Validation. **Xiaoyu Feng:** Visualization. **Yushu Wang:** Methodology. **Lixia Yu:** Investigation, Formal analysis. **Ying Chen:** Supervision, Methodology. **Rutian Li:** Writing – review & editing, Supervision, Methodology, Funding acquisition, Conceptualization.

Declaration of competing interest

The authors declare that they have no known competing financial interests or personal relationships that could have appeared to influence the work reported in this paper.

Data availability

Data will be made available on request.

Appendix A. Supplementary data

Supplementary data to this article can be found online at https://doi.org/10.1016/j.mtbio.2024.101281.

References

[1] I. Melero, E. Castanon, M. Alvarez, et al., Intratumoural administration and tumour tissue targeting of cancer immunotherapies, Nat. Rev. Clin. Oncol. 18 (9) (2021) 558–576.

[2] J.M. Llovet, F. Castet, M. Heikenwalder, et al., Immunotherapies for hepatocellular carcinoma, Nat. Rev. Clin. Oncol. 19 (3) (2021) 151–172.

[3] A. Kanani, T. Veen, K. SøREIDE, Neoadjuvant immunotherapy in primary and metastatic colorectal cancer, Br. J. Surg. 108 (12) (2021) 1417–1425.

[4] A. Harari, M. Graciotti, M. Bassani-Sternberg, et al., Antitumour dendritic cell vaccination in a priming and boosting approach, Nat. Rev. Drug Discov. 19 (9) (2020) 635–652.

[5] M.L. Disis, K.A. Guthrie, Y. Liu, et al., Safety and outcomes of a plasmid DNA vaccine encoding the ERBB2 intracellular domain in patients with advanced-stage ERBB2-positive breast cancer, JAMA Oncol. 9 (1) (2023).

[6] L. Miao, Y. Zhang, L. Huang, mRNA vaccine for cancer immunotherapy, Mol. Cancer 20 (1) (2021).

[7] W. Liu, H. Tang, L. Li, et al., Peptide-based therapeutic cancer vaccine: current trends in clinical application, Cell Prolif. 54 (5) (2021).

[8] W. Liu, E. Dai, Z. Liu, et al., In situ therapeutic cancer vaccination with an oncolytic virus expressing membrane-tethered IL-2, Mol Ther Oncolytics 17 (2020) 350–360.

[9] A. Redenti, J. Hahn, T. Danino, Bacterial couriers as cancer vaccines, Nat. Biomed. Eng. 6 (1) (2022) 3–5.

[10] J. Chen, Z. Jin, S. Zhang, et al., Arsenic trioxide elicits prophylactic and therapeutic immune responses against solid tumors by inducing necroptosis and ferroptosis, Cell. Mol. Immunol. 20 (1) (2022) 51–64.

[11] H. Xu, H. Zhao, C. Ding, et al., Celastrol suppresses colorectal cancer via covalent targeting peroxiredoxin 1, Signal Transduct. Targeted Ther. 8 (1) (2023).

[12] M. Hu, H. Yan, H. Li, et al., Use of network pharmacology and molecular docking to explore the mechanism of action of curcuma in the treatment of osteosarcoma, Sci. Rep. 13 (1) (2023).

[13] Y.-S. Wang, Y. Lin, H. Li, et al., The identification of molecular target of (20S) ginsenoside Rh2 for its anti-cancer activity, Sci. Rep. 7 (1) (2017) 12408.

[14] N.H. Yim, Y.S. Kim, H.S. Chung, Inhibition of programmed death receptor-1/programmed death ligand-1 interactions by ginsenoside metabolites, Molecules 25 (9) (2020).

[15] M. Hamidi, A. Azadi, P. Rafiei, Hydrogel nanoparticles in drug delivery, Adv. Drug Deliv. Rev. 60 (15) (2008) 1638–1649.

[16] L. Lei, D. Huang, H. Gao, et al., Hydrogel-guided strategies to stimulate an effective immune response for vaccine-based cancer immunotherapy, Sci. Adv. 8 (47) (2022).

[17] Y. Ke, J. Zhu, Y. Chu, et al., Bifunctional fusion membrane-based hydrogel enhances antitumor potency of autologous cancer vaccines by activating dendritic cells 32 (29) (2022) 2201306.

[18] Y. Li, Y. Zhu, S. Luo, et al., Redox-sensitive ultrashort peptide hydrogel with tunable mechanical properties for anti-tumor drug delivery, J. Biomed. Nanotechnol. 16 (11) (2020) 1588–1599.

[19] K. Yamaguchi, O. Hiraike, H. Iwaki, et al., Intraperitoneal administration of a cisplatin-loaded nanogel through a hybrid system containing an alginic acid-based nanogel and an in situ cross-linkable hydrogel for peritoneal dissemination of ovarian cancer, Mol. Pharm. 18 (11) (2021) 4090–4098.

[20] F. Wang, J. Chen, J. Liu, et al., Cancer theranostic platforms based on injectable polymer hydrogels, Biomater. Sci. 9 (10) (2021) 3543–3575.

[21] Y. Yin, W. Feng, J. Chen, et al., Immunosuppressive tumor microenvironment in the progression, metastasis, and therapy of hepatocellular carcinoma: from bench to bedside, Exp. Hematol. Oncol. 13 (1) (2024).

[22] L.F. Mager, M.-H. Wasmer, T.T. Rau, et al., Cytokine-induced modulation of colorectal cancer, Front. Oncol. 6 (2016).

[23] Q. Li, J. He, S. Li, et al., The combination of gemcitabine and ginsenoside Rh2 enhances the immune function of dendritic cells against pancreatic cancer via the CARD9-BCL10-MALT1/NF-kappaB pathway, Clin Immunol 248 (2023) 109217.

[24] C. Song, H. Phuengkham, Y.S. Kim, et al., Syringeable immunotherapeutic nanogel reshapes tumor microenvironment and prevents tumor metastasis and recurrence, Nat. Commun. 10 (1) (2019) 3745.

[25] H. Li, N. Huang, W. Zhu, et al., Modulation the crosstalk between tumor-associated macrophages and non-small cell lung cancer to inhibit tumor migration and invasion by ginsenoside Rh2, BMC Cancer 18 (1) (2018) 579.

[26] F. Markl, D. Huynh, S. Endres, et al., Utilizing chemokines in cancer immunotherapy, Trends Cancer 8 (8) (2022) 670–682.

[27] D.J. Propper, F.R. Balkwill, Harnessing cytokines and chemokines for cancer therapy, Nat. Rev. Clin. Oncol. 19 (4) (2022) 237–253.

[28] J. Zhou, Y. Shi, Mesenchymal stem/stromal cells (MSCs): origin, immune regulation, and clinical applications, Cell. Mol. Immunol. 20 (6) (2023) 555–557.

[29] S. Vijayan, T. Sidiq, S. Yousuf, et al., Class I transactivator, NLRC5: a central player in the MHC class I pathway and cancer immune surveillance, Immunogenetics 71 (3) (2019) 273–282.

[30] C. Yamada, T. Ozaki, K. Ando, et al., RUNX3 modulates DNA damage-mediated phosphorylation of tumor suppressor p53 at Ser-15 and acts as a co-activator for p53, J. Biol. Chem. 285 (22) (2010) 16693–16703.

[31] C. Xie, F. Ye, N. Zhang, et al., CCL7 contributes to angiotensin II-induced abdominal aortic aneurysm by promoting macrophage infiltration and pro-inflammatory phenotype, J. Cell Mol. Med. 25 (15) (2021) 7280–7293.

[32] H. Harjunpaa, M. Llort Asens, C. Guenther, et al., Cell adhesion molecules and their roles and regulation in the immune and tumor microenvironment, Front. Immunol. 10 (2019) 1078.

[33] X. Li, Z. Sun, J. Ma, et al., Identification of TNFRSF21 as an inhibitory factor of osteosarcoma based on a necroptosis-related prognostic gene signature and molecular experiments, Cancer Cell Int. 24 (1) (2024) 14.

[34] X. Xia, J. Tao, Z. Ji, et al., Increased antitumor efficacy of ginsenoside Rh2 via mixed micelles: in vivo and in vitro evaluation, Drug Deliv. 27 (1) (2020) 1369–1377.

[35] B. Allard, D. Allard, J. Stagg, Methods to evaluate the antitumor activity of immune checkpoint inhibitors in preclinical studies, Methods Mol. Biol. 1458 (2016) 159–177.

[36] J.S. Ni, X. Zhang, G. Yang, et al., A photoinduced nonadiabatic decay-guided molecular motor triggers effective photothermal conversion for cancer therapy, Angew Chem. Int. Ed. Engl. 59 (28) (2020) 11298–11302.